

## Advection-reaction-diffusion coupled with viscous flow in a peridynamic framework

Zhaoyang Song <sup>a</sup>, Chenwen Tian <sup>a</sup>, Juan Du <sup>b</sup>, Florin Bobaru <sup>c</sup>, Ziguang Chen <sup>a,d,\*</sup>

<sup>a</sup> Department of Engineering Mechanics, Huazhong University of Science and Technology, Wuhan, 430074, China

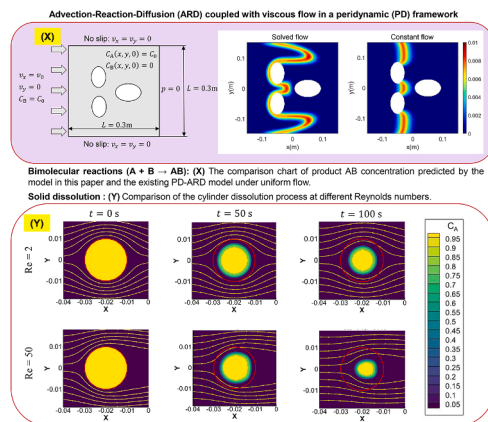
<sup>b</sup> National Key Laboratory of Nuclear Reactor Technology, Nuclear Power Institute of China, Chengdu 610213, China

<sup>c</sup> Department of Mechanical and Materials Engineering, University of Nebraska-Lincoln, Lincoln, NE, 68588-0526, USA

<sup>d</sup> Hubei Key Laboratory of Engineering Structural Analysis and Safety Assessment, 1037 Luoyu Road, Wuhan, 430074, China



### GRAPHICAL ABSTRACT



### ARTICLE INFO

#### Keywords:

Peridynamics  
Advection-reaction-diffusion  
Viscous flow  
Weakly compressible flow  
Contaminated water flow  
Solid dissolution

### ABSTRACT

This paper introduces a Peridynamic (PD) model for simulating the Advection-Reaction-Diffusion (ARD) processes in a non-uniform flow. The ARD phenomena are influenced by the flow, and the flow is modified by phase-changes (driven by interface reactions) that transform the boundaries of solids in the flow, for example. By coupling the PD governing equations for viscous flow with the PD equations for ARD, the model facilitates the effective simulation of the ARD process in viscous flow within the PD framework. The results demonstrate a high level of agreement with

\* Corresponding author.

E-mail address: [zchen@hust.edu.cn](mailto:zchen@hust.edu.cn) (Z. Chen).

COMSOL simulations for ARD problems in two-dimensional flow, both in the presence and absence of obstacles. Furthermore, the framework demonstrates remarkable versatility in addressing complex scenarios, including ARD processes in heterogeneous media and flow-accelerated solid dissolution dynamics. These capabilities open new avenues for applications in critical areas such as groundwater contaminant transport, karst formation through rock dissolution, targeted drug delivery systems in biological environments, and other types of material degradation through phase-changes under fluid flow conditions, like ice melting and ablation.

## 1. Introduction

The Advection-Reaction-Diffusion (ARD) process is a fundamental phenomenon observed in diverse systems, ranging from drug transport in biological tissues [1,2] and pollutant dispersion in groundwater systems [3] to the propagation of infectious diseases across complex networks [4]. While analytical solutions exist for certain special cases of the classical ARD equations, the majority of practical problems require numerical approximations due to their inherent complexity [5–7]. However, classical ARD models [8–10] exhibit two significant limitations. First, the core assumption of locality in PDEs means they cannot naturally handle discontinuities such as phase interfaces [11], fracture networks [12,13], damage zones or evolving material interfaces [14,15]. Modeling these phenomena requires complex add-ons like cohesive zone models [16], phase-field models [17] or the eXtended Finite Element Method (XFEM) [18], which may require a priori knowledge of the path or can introduce non-physical artifacts. Second, this assumption of locality breaks down in systems with significant long-range interactions or microscale heterogeneities, such as anomalous transport in porous media [19–21], the collective behavior of animals [22,23] or cell-to-cell signaling [22,24], which are inherently non-local.

Peridynamics (PD), a nonlocal continuum theory introduced by Silling in 2000 [25], presents a paradigm shift by replacing spatial derivatives with integral operators and introducing the concept of nonlocal interactions over a "horizon region". PD does not require smoothness of the unknown function, making it well-suited for handling spontaneous discontinuities in the solution at points in the continuum domain [26,27]. The absence of spatial derivatives in the PD formulation, and presence of a spatial length-scale (the nonlocal region of interaction) removes the singularities that arise at contact points or at points where material separation happened in the classical theories [28]. This theory has been successfully applied to simulate various physical phenomena, including material damage [29–32], hydraulic fracturing [33], thermal diffusion [34], fatigue failure [35,36], and plastic deformation and ductile damage [37–40]. As such, PD addresses the two primary limitations of classical ARD models: it naturally accommodates evolving interfaces without predefined assumptions [41] and inherently incorporates long-range effects and microscale heterogeneities [29, 42–44].

The application of PD to transport phenomena has progressed systematically, from diffusion-only processes to ARD simulations [45–47]. However, these advanced PD-ARD models have been confined by a critical and highly idealized assumption: that transport occurs within a uniform, constant-velocity flow field [47]. This simplification represents a significant gap, as most critical applications involve complex, non-uniform, and dynamically evolving fluid flows. Addressing this requires a fully-coupled model where the fluid dynamics and the ARD process influence each other. To address this gap, we propose the PD-ARD equation for non-uniform flow conditions. This equation requires the flow field as input parameters. While the flow field can be solved using traditional fluid mechanics models discretized using the finite element method (FEM), this would eliminate the natural advantage of PD, which does not require predefining the function for the evolution of the interface. Moreover, the fundamental differences between PD and classical continuum mechanics present significant coupling challenges. In most previous studies, the Peridynamic Differential Operator (PDDO) [48], a non-local numerical method, has been used to solve the local equations of classical Navier-Stokes equations (NSEs) [49,50], which are still fundamentally local. Recently, Zhao et al. derived a particular case of the NSEs for the PD model of Newtonian viscous flow based on the basic principles of mass and momentum conservation [51], which is non-local in nature. The method used to enforce wall boundary conditions in [51] could lead to the velocities with the non-physical component perpendicular to the wall, instead of one that is purely tangent to the complex wall geometry. Here we resolve this issue by allowing the density of virtual nodes to evolve naturally over time. This creates a pressure-based resistance, which implicitly enforces the impermeability condition (see [Appendix D](#) and [Section 3.2](#)). The formulation in [51] is also only stable for low Reynolds number flows and we show that it suffers from non-physical oscillations at higher Reynolds numbers. In the present work we incorporate a density diffusion term that reduces such oscillations. We couple this improved PD NSEs model for viscous flow with the PD equations for ARD, allowing us to model ARD phenomena in non-uniform viscous flow. The seamless integration of these advanced components yields a unified, self-consistent, and robust framework capable of addressing key challenges such as karst formation simulation, drug delivery and release, groundwater contamination remediation, and electrochemical interfacial mass transport.

The remainder of this paper is organized as follows: [Section 2](#) presents the modified PD formulation for the NSEs and the new coupled model of these equations with the PD-ARD equations. [Section 3](#) introduces the numerical methods used for discretization and the application of boundary conditions. In [Section 4](#), we verify the model and boundary conditions by comparing the results with those from COMSOL obtained for the corresponding classical problem and apply the model to ARD problems in non-uniform fluid flow and complex geometries with multiple obstacles and to flow-induced solid dissolution. Finally, conclusions are drawn in [Section 5](#).

## 2. PD-ARD model for viscous flow

By replacing the advection term in the PD-ARD equation from [47] with the general PD continuity equation in the Eulerian framework [51], the following equation is obtained:

$$\frac{\partial C_p(\mathbf{x}, t)}{\partial t} = \int_{\mathcal{H}_x} d(\mathbf{x}, \hat{\mathbf{x}}, t) \frac{C_p(\hat{\mathbf{x}}, t) - C_p(\mathbf{x}, t)}{\|\hat{\mathbf{x}} - \mathbf{x}\|^2} d\hat{\mathbf{x}} - \int_{\mathcal{H}_x} \frac{\alpha}{V_{\mathcal{H}_x}} \frac{C_p(\hat{\mathbf{x}}, t)\mathbf{v}(\hat{\mathbf{x}}, t) - C_p(\mathbf{x}, t)\mathbf{v}(\mathbf{x}, t)}{\|\hat{\mathbf{x}} - \mathbf{x}\|} \cdot \mathbf{e}(\mathbf{x}, \hat{\mathbf{x}}) d\hat{\mathbf{x}} + \sum_{q=1}^{M_p} R_{pq}(\mathbf{x}, t) \quad (1)$$

where  $C_p(\mathbf{x}, t)$  represent the concentration of the  $p$ -th species at time  $t$  at the point  $\mathbf{x}$ .  $\mathcal{H}_x$  denotes the horizon region of  $\mathbf{x}$ . In the PD model, each substance point  $\mathbf{x} \in \Omega$  interacts with other points within its horizon region (see Fig. 1), which is typically a circular disk in two dimensions (sphere in 3D) with a radius  $\delta$ .  $V_{\mathcal{H}_x}$  is the area covered by  $\mathcal{H}_x$  (volume in 3D). The velocity vector of material point  $\mathbf{x}$  at time  $t$  is represented by  $\mathbf{v}(\mathbf{x}, t)$ , and  $\mathbf{e}(\mathbf{x}, \hat{\mathbf{x}})$  is the unit "bond vector" in the direction from  $\mathbf{x}$  to  $\hat{\mathbf{x}}$ .  $R_{pq}(\mathbf{x}, t)$  denotes the  $q$ -th reaction of the  $p$ -th species. The  $p$ -th species is involved in  $M_p$  reactions with other species, so the range of values of  $q$  can be expressed in mathematical symbols as  $q \in [1, M_p]$ . Depending on the role a substance plays in a given reaction, such as being a product or reactant, the corresponding reaction rate can be either positive or negative. The constant  $\alpha$  establishes the link between the macroscale flow velocity and the bond-level flow velocity, and its value is equal to the dimension (for example,  $\alpha = 2$  in 2D, as discussed in [51]). We define the projections of the velocity in the direction of  $\mathbf{e}(\mathbf{x}, \hat{\mathbf{x}})$  as:  $\hat{\mathbf{v}} = \frac{\alpha}{\pi\delta^2} \hat{\mathbf{v}} \cdot \mathbf{e}(\mathbf{x}, \hat{\mathbf{x}})$ ,  $v = \frac{\alpha}{\pi\delta^2} \mathbf{v} \cdot \mathbf{e}(\mathbf{x}, \hat{\mathbf{x}})$ . For the micro-diffusivity function  $d(\mathbf{x}, \hat{\mathbf{x}}, t)$ , the relationship between the macroscopic diffusion coefficient and the microscopic diffusion coefficient is established. Two common forms for this function are the "constant" and "triangular/conical" types, given by:  $d(\mathbf{x}, \hat{\mathbf{x}}, t) = d_0$  and  $d(\mathbf{x}, \hat{\mathbf{x}}, t) = d_1 \left(1 - \frac{\|\mathbf{x} - \hat{\mathbf{x}}\|}{\delta}\right)$ , respectively. Based on the matching of the PD model with the classical model in cases where the concentration distribution of a substance in solution is linear, it can be concluded that, in the two-dimensional case,  $d_0 = 4D/\pi\delta^2$  and  $d_1 = 12D/\pi\delta^2$ , where  $D$  is the diffusion coefficient. In Eq. (1), we set  $d(\mathbf{x}, \hat{\mathbf{x}}, t) = d_0$ .

For the advection part in Eq. (1), three schemes are considered (see Fig. 2): the central scheme, the upwind scheme [46], and the downwind scheme. As demonstrated in [46], the central scheme offers higher accuracy than the upwind scheme but is numerically less stable than the upwind scheme. Since the downwind scheme performs slightly better than the upwind scheme in the examples presented in this paper, we use the downwind scheme uniformly for simplicity. The specific features and performance of the downwind and upwind scheme are not the main focus of this paper. Similar to the approach in [46], the advection term in this study employs a hybrid scheme, combining the central and downwind scheme as follows:

$$\begin{aligned} \frac{\partial C_p(\mathbf{x}, t)}{\partial t} &= \int_{\mathcal{H}_x} d(\mathbf{x}, \hat{\mathbf{x}}, t) \frac{C_p(\hat{\mathbf{x}}, t) - C_p(\mathbf{x}, t)}{\|\hat{\mathbf{x}} - \mathbf{x}\|^2} d\hat{\mathbf{x}} - w \int_{\mathcal{H}_x} \frac{C_p(\hat{\mathbf{x}}, t)\mathbf{v}(\hat{\mathbf{x}}, t) - C_p(\mathbf{x}, t)\mathbf{v}(\mathbf{x}, t)}{\|\hat{\mathbf{x}} - \mathbf{x}\|} d\hat{\mathbf{x}} \\ &\quad - (1 - w) \int_{\mathcal{H}_x} \frac{C_p(\hat{\mathbf{x}}, t)\tilde{\mathbf{v}}(\hat{\mathbf{x}}, t) - C_p(\mathbf{x}, t)\tilde{\mathbf{v}}(\mathbf{x}, t)}{\|\hat{\mathbf{x}} - \mathbf{x}\|} d\hat{\mathbf{x}} + \sum_{q=1}^{M_p} R_{pq}(\mathbf{x}, t) \end{aligned} \quad (2)$$

where  $\tilde{\mathbf{v}}(\hat{\mathbf{x}}, t) = \frac{\beta}{\pi\delta^2} \mathbf{v}(\hat{\mathbf{x}}, t) \cdot \mathbf{e}(\mathbf{x}, \hat{\mathbf{x}})$ ,  $\tilde{\mathbf{v}}(\mathbf{x}, t) = \frac{\beta}{\pi\delta^2} \mathbf{v}(\mathbf{x}, t) \cdot \mathbf{e}(\mathbf{x}, \hat{\mathbf{x}})$ ,  $\beta$  is the coefficient connecting the macroscale flow velocity and the bond-level flow velocity in the downwind scheme, and for simplicity,  $\beta$  is treated as a constant. When the flow field is uniform,  $\beta = 2\alpha$  is obtained by comparing with the PD-ARD equation in [47].  $\mathcal{H}_x$  represents the downwind portion of the horizon. The selection of a suitable  $w$  can help mitigate numerical instabilities and numerical diffusion. The value of  $w$  is selected based on the Peclet number  $\text{Pe} = VL/D$  (see [52]). Since the Peclet number in this study is similar to that in [47], for convenience, we adopt the same value for  $w = 0.8$  as in [47].

At this point, the PD-ARD equation under non-uniform flow has been established. Unless otherwise specified, the PD-ARD model/equation mentioned hereafter specifically refers to the PD model for coupled ARD in a viscous flow phenomenon, proposed in this

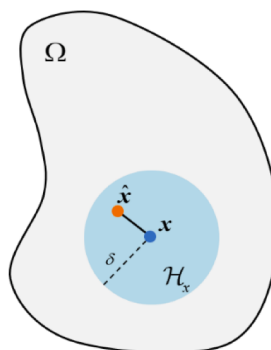


**Fig. 1.** A schematic diagram illustrating the interaction of a material point  $\mathbf{x}$  with other material points  $\hat{\mathbf{x}}$  within its horizon region.

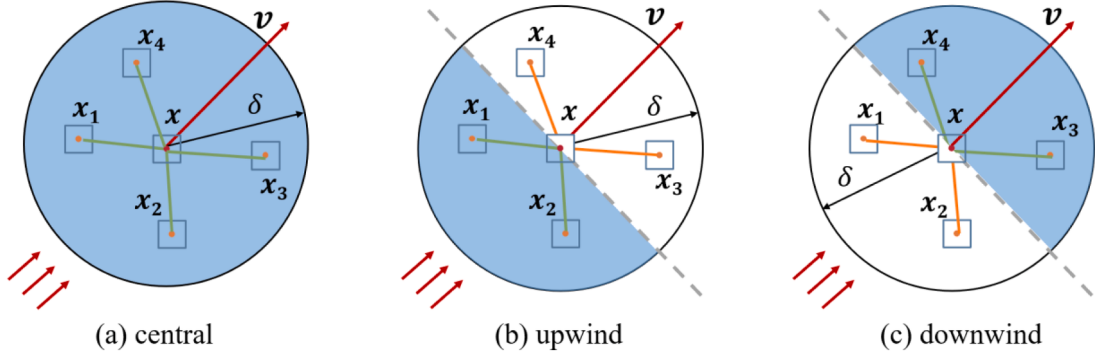


Fig. 2. Central kernel, upwind kernel and downwind kernel under a flow field that induces velocity  $\mathbf{v}$  at  $\mathbf{x}$ .

work.

The weakly compressible method used in [51] avoids the numerical difficulties associated with directly solving the original incompressible equations in terms of accuracy and efficiency. However, this method inevitably leads to pressure/density oscillations in numerical calculation. This issue is particularly pronounced when acoustic waves interact with boundaries (e.g., solid walls or inlet/outlet boundaries), where the energy of reflected waves cannot be effectively dissipated, resulting in stronger pressure/density oscillations [53,54]. These oscillations significantly affect the stability of the algorithm. To mitigate these numerical oscillations, we adopt an approach similar to that in [50], wherein a density diffusion term is introduced into the continuity equation:

$$\frac{\partial \rho(\mathbf{x}, t)}{\partial t} = -\frac{\alpha}{V_{\mathcal{K}}} \int_{\mathcal{K}_x} \frac{\hat{\rho} \hat{\mathbf{v}} - \rho \mathbf{v}}{\|\hat{\mathbf{x}} - \mathbf{x}\|} \cdot \mathbf{e} d\hat{\mathbf{x}} + \eta \int_{\mathcal{K}_x} k(\mathbf{x}, \hat{\mathbf{x}}, t) \frac{\hat{\rho} - \rho}{\|\hat{\mathbf{x}} - \mathbf{x}\|^2} d\hat{\mathbf{x}} \quad (3)$$

$$\begin{aligned} \frac{\partial(\rho(\mathbf{x}, t)\mathbf{v}(\mathbf{x}, t))}{\partial t} &= -\frac{\alpha}{V_{\mathcal{K}}} \int_{\mathcal{K}_x} \frac{\hat{\rho} \hat{\mathbf{v}} \otimes \hat{\mathbf{v}} - \rho \mathbf{v} \otimes \mathbf{v}}{\|\hat{\mathbf{x}} - \mathbf{x}\|} \cdot \mathbf{e} d\hat{\mathbf{x}} - \frac{\alpha_p}{V_{\mathcal{K}}} \int_{\mathcal{K}_x} \frac{\hat{p} - p}{\|\hat{\mathbf{x}} - \mathbf{x}\|} \cdot \mathbf{e} d\hat{\mathbf{x}} \\ &\quad + \frac{\mu \alpha_\mu}{V_{\mathcal{K}}} \int_{\mathcal{K}_x} \frac{((\mathbf{I} - \mathbf{e} \otimes \mathbf{e})(\hat{\mathbf{v}} - \mathbf{v}))}{\|\hat{\mathbf{x}} - \mathbf{x}\|^2} d\hat{\mathbf{x}} + \rho \mathbf{b} \end{aligned} \quad (4)$$

where  $\hat{\rho}$  represents the shorthand for  $\rho(\hat{\mathbf{x}}, t)$ , the density at the material point  $\hat{\mathbf{x}}$  at time  $t$ ,  $\hat{p}$  is the pressure at the material point  $\hat{\mathbf{x}}$  at time  $t$ , and  $\mathbf{b}$  is the given force density at the material point  $\mathbf{x}$  at time  $t$ .  $\mathbf{e}$  is shorthand for  $\mathbf{e}(\mathbf{x}, \hat{\mathbf{x}})$ ,  $\mu$  is the fluid viscosity, and  $\alpha_p$  is a constant whose value is equal to the dimension [51] (since all discussions in this paper are in the two-dimensional case,  $\alpha_p = 2$ ). The value of  $\alpha_\mu$  is determined from a simple flow problem, ensuring the linear consistency of the formulation [46,55], which gives  $\alpha_\mu = 16/3$  for the 2D case.  $\eta$  is a correction factor, typically set to 0.1, and  $k(\mathbf{x}, \hat{\mathbf{x}}, t)$  is a micro-diffusion function related to the density, with the magnitude of the diffusion coefficient being  $D_\rho = c_0 \delta$ . Similar to the possible choices for the “shape” of the  $d(\mathbf{x}, \hat{\mathbf{x}}, t)$  function, mentioned earlier, one can choose the “constant” or “triangular” options for representing  $k(\mathbf{x}, \hat{\mathbf{x}}, t)$ . Here, for simplicity, we select  $k(\mathbf{x}, \hat{\mathbf{x}}, t)$  to be of “constant” type:  $k(\mathbf{x}, \hat{\mathbf{x}}, t) = 4D_\rho/\pi\delta^2$ . Note that Chang et al [50] use two methods to reduce numerical instabilities and increase accuracy: artificial viscosity and density diffusion. Here we notice that using the density diffusive term alone is sufficient to eliminate the non-physical oscillations in pressure from the solution. Numerical experiments show that the density diffusive term effectively reduces numerical oscillations, thus improving the stability of the method (see Appendix A for numerical oscillations). Furthermore, it is important to note that for the flow field Eqs. (3) and (4), we utilize a central scheme, in contrast to the hybrid scheme employed in the PD-ARD equation. This choice is motivated by the fact that a down-wind scheme exhibits unconditional instability when applied to the one-dimensional linear convection equation (a simplified form of the mass conservation Eq. (3)) within the peridynamic framework, as demonstrated in Appendix B.

We also need an additional equation of state to establish the relationship between pressure and density. Here, we adopt the equation of state used in [51] for weakly compressible fluids:

$$p = \frac{\rho_0 c_0^2}{\gamma} \left( \left( \frac{\rho^*}{\rho_0} \right)^\gamma - 1 \right) \quad (5)$$

where  $\rho_0$  is the initial density,  $\rho^*$  is the predicted density at the current step,  $\gamma$  is a material constant, which is 7 for water [51], and  $c_0$  is the artificial speed of sound. The selection of artificial sound speed should take into account two limitations: on one hand, the sound speed must be at least 10 times greater than the maximum flow velocity to ensure that the density variation of the fluid remains within 1 % of its initial density (i.e., the Mach number,  $M = v/c_0$ , must be less than 0.1 [56]); on the other hand, the sound speed should not be too high, as excessively high sound speeds would result in a very small time step (see Section 3.1).

### 3. Numerical implementation

Section 3.1 explains the discretization of the new PD-ARD model and outlines the associated stability conditions. Section 3.2 details the boundary conditions used in this study, including the pressure outlet boundary condition, the velocity inlet boundary condition, and the no-slip solid wall boundary condition.

#### 3.1. Numerical discretization

In this study, a uniform grid with a grid spacing of  $\Delta x$  is used to discretize the entire computational domain, and the integral term is approximated using mid-point integration (or one-point Gaussian quadrature) [57]. Non-uniform grids can also be used [58–60], and those conforming to non-straight boundaries have a series of advantages (see [42,61]). Here, for simplicity, we use uniform grids only.

In 3D problems, the mid-point quadrature for the nonlocal operators becomes expensive and other options can be more efficient (see [62–64]). Because here we limit ourselves to examples in 2D, the mid-point quadrature is chosen to approximate the integral terms in the PD equation. For the time derivative, we select the forward Euler method, for simplicity.

With these discretizations, the PD-ARD coupled equations (Eqs. (1), (3), and (4)) can be written as:

$$\rho_i^{n+1} = \rho_i^n + \Delta t \left[ -\frac{\alpha}{\pi \delta^2} \sum_{\substack{j \in \mathcal{N}_i \\ j \neq i}} \left( \frac{\rho_j^n \mathbf{v}_j^n - \rho_i^n \mathbf{v}_i^n}{\xi_{ij}} \cdot \mathbf{e}_{ij} V_{ij} \right) + \eta \frac{4D_p}{\pi \delta^2} \sum_{\substack{j \in \mathcal{N}_i \\ j \neq i}} \left( \frac{\rho_j^n - \rho_i^n}{\xi_{ij}^2} V_{ij} \right) \right] \quad (6)$$

$$\begin{aligned} \mathbf{v}_i^{n+1} = \mathbf{v}_i^n + \frac{\Delta t}{\rho_i^n} \left[ -\frac{\alpha}{V_{\mathcal{N}}} \left( \sum_{\substack{j \in \mathcal{N}_i \\ j \neq i}} \frac{(\rho_j^n \mathbf{v}_j^n \otimes \mathbf{v}_j^n - \rho_i^n \mathbf{v}_i^n \otimes \mathbf{v}_i^n)}{\xi_{ij}} \cdot \mathbf{e}_{ij} V_{ij} \right) - \frac{\alpha_p}{V_{\mathcal{N}}} \sum_{\substack{j \in \mathcal{N}_i \\ j \neq i}} \left( \frac{(p_j^n - p_i^n) \xi_{ij}}{\xi_{ij}^2} V_{ij} \right) \right. \\ \left. + \frac{\mu \alpha_\mu}{V_{\mathcal{N}}} \sum_{\substack{j \in \mathcal{N}_i \\ j \neq i}} \frac{1}{\xi_{ij}^2} \left( \mathbf{I} - \frac{\xi_{ij} \otimes \xi_{ij}}{\xi_{ij}^2} \right) \cdot (\mathbf{v}_j^n - \mathbf{v}_i^n) V_{ij} + \rho_i^n \mathbf{b}_i^n \right] \end{aligned} \quad (7)$$

$$C_p^{n+1}(\mathbf{x}_i, t) = C_p^n(\mathbf{x}_i, t) + \Delta t \left[ d_0 \sum_{\substack{j \in \mathcal{N}_i \\ j \neq i}} \left( \frac{C_p^n(\mathbf{x}_j, t) - C_p^n(\mathbf{x}_i, t)}{\xi_{ij}^2} V_{ij} \right) \right. \\ \left. - \sum_{\substack{j \in \mathcal{N}_i \\ j \neq i}} \left( \frac{C_p^n(\mathbf{x}_j, t) v^n(\mathbf{x}_j, t) - C_p^n(\mathbf{x}_i, t) v^n(\mathbf{x}_i, t)}{\xi_{ij}^2} V_{ij} \right) + \sum_{q=1}^{M_p} R_{pq}(\mathbf{x}_i, t) + Q_{d,ii} + Q_{v,ii} \right] \quad (8)$$

where  $e_{ij} = \frac{\mathbf{x}_j - \mathbf{x}_i}{\|\mathbf{x}_j - \mathbf{x}_i\|}$  is the unit direction vector of the PD bond vector  $\xi_{ij} = \mathbf{x}_j - \mathbf{x}_i$ ,  $\xi_{ij} = \|\mathbf{x}_j - \mathbf{x}_i\|$ .  $V_{ij}$  represents the volume of node  $\mathbf{x}_j$  covered by the horizon region of node  $\mathbf{x}_i$ . When the entire node  $\mathbf{x}_j$  is within the horizon region of node  $\mathbf{x}_i$ ,  $V_{ij} = \Delta x^2$ . If only a portion of the volume of  $\mathbf{x}_j$  lies within the horizon of node  $\mathbf{x}_i$ , the HBB algorithm [27,65] is used to approximate  $V_{ij}$ .  $V_{ij}$  can also be calculated based on the probability of interaction between  $\mathbf{x}_i$  and  $\mathbf{x}_j$  [66]. The superscript  $n$  denotes the  $n$ -th time step, with a step size of  $\Delta t$ .  $Q_{d,ii}$  represents the flux diffused by node  $\mathbf{x}_i$  within its own volume when  $j = i$ , and  $Q_{v,ii}$  represents the flux due to convection within its own volume when  $j = i$ . The specific rationale for the presence of these two terms is detailed in Appendix C. To ensure that substances do not interpenetrate, we calculate the values of these terms by using the nearest neighbors of the node [46].

For the central scheme (see Fig. 2) (considering the nearest eight nodes around node  $\mathbf{x}_i$ , as first suggested in [55,67]) we have:

$$Q_{d,ii} = \frac{1}{8} \sum_{j=1}^8 \left( d_0 \frac{C_p(\mathbf{x}_j, t) - C_p(\mathbf{x}_i, t)}{\|\mathbf{x}_j - \mathbf{x}_i\|^2} V_{ij} \right) \quad (9)$$

$$Q_{v,ii} = -\frac{1}{8} \sum_{j=1}^8 \left( \frac{C_p(\mathbf{x}_j, t)v(\mathbf{x}_j, t) - C_p(\mathbf{x}_i, t)v(\mathbf{x}_i, t)}{\|\mathbf{x}_j - \mathbf{x}_i\|} V_{ij} \right), \quad (10)$$

while for the upwind/downwind scheme, we get:

$$Q_{v,ii} = -\frac{1}{3} \sum_{j=1}^3 \left( \frac{C_p(\mathbf{x}_j, t)v(\mathbf{x}_j, t) - C_p(\mathbf{x}_i, t)v(\mathbf{x}_i, t)}{\|\mathbf{x}_j - \mathbf{x}_i\|} V_{ij} \right). \quad (11)$$

For the computational stability analysis of the discrete Eq. (8), the von Neumann stability analysis [57] is used in this paper. It is assumed that the error can be written in the form of a Fourier transform:

$$\epsilon_j^n = \epsilon^n e^{kj\sqrt{-1}} \quad (12)$$

where  $\epsilon_j^n$  denotes the error at node  $j$  at time step  $n$ . Introducing this error function into Eq. (8), and excluding the reaction term from this stability analysis since it does not impact computational stability and only influences the accuracy, we get:

$$\|\epsilon\| = \|1 + \Delta t \left[ \sum_{j \in \mathcal{N}_i} \left( d_0 \frac{e^{k(j-i)\sqrt{-1}} - 1}{\|\mathbf{x}_j - \mathbf{x}_i\|^2} V_{ij} \right) - \sum_{j \in \mathcal{N}_i} \left( \frac{e^{k(j-i)\sqrt{-1}} v_j - v_i}{\|\mathbf{x}_j - \mathbf{x}_i\|} V_{ij} \right) \right]\| \leq 1 \quad (13)$$

For the central scheme, by substituting Euler's formula  $e^{w\sqrt{-1}} = \cos w + \sqrt{-1} \sin w$  into Eq. (13), we can obtain:

$$\|\epsilon\| = \|1 + \Delta t \left[ \sum_{j \in \mathcal{N}_i} \left( \frac{d_0 (\cos(k(j-i)) - 1)}{\|\mathbf{x}_j - \mathbf{x}_i\|^2} V_{ij} \right) - \sum_{j \in \mathcal{N}_i} \left( \frac{v_j \cos(k(j-i))}{\|\mathbf{x}_j - \mathbf{x}_i\|} V_{ij} \right) - \sqrt{-1} \sum_{j \in \mathcal{N}_i} \left( \frac{v_j \sin(k(j-i))}{\|\mathbf{x}_j - \mathbf{x}_i\|} V_{ij} \right) \right]\| \leq 1 \quad (14)$$

As indicated by Eq. (14), when  $\operatorname{Re}(\epsilon) - 1 \geq 0$ , the computation process will enter an unconditionally unstable state; therefore, it is assumed that  $\operatorname{Re}(\epsilon) - 1 \leq 0$  here. A sufficient condition for  $\|\epsilon\| \leq 1$  to hold is that  $|\operatorname{Re}(\epsilon)| \leq 1/2$  and  $|\operatorname{Im}(\epsilon)| \leq 1/2$ . Furthermore, this sufficient condition can be expressed as:

$$\begin{cases} \frac{1}{2} \leq \Delta t \sum_{j \in \mathcal{N}_i} \left( \frac{d_0 (1 - \cos(k(j-i)))}{\|\mathbf{x}_j - \mathbf{x}_i\|^2} V_{ij} \right) + \Delta t \sum_{j \in \mathcal{N}_i} \left( \frac{v_j \cos(k(j-i))}{\|\mathbf{x}_j - \mathbf{x}_i\|} V_{ij} \right) \leq \frac{3}{2} \\ \Delta t \left| \sum_{j \in \mathcal{N}_i} \left( \frac{v_j \sin(k(j-i))}{\|\mathbf{x}_j - \mathbf{x}_i\|} V_{ij} \right) \right| \leq \frac{1}{2} \end{cases} \quad (15)$$

In numerical computations, smaller  $\Delta t$  generally leads to a more stable calculation process; therefore, no restriction on the lower bound of  $\Delta t$  is typically required. Consequently, for the first inequality in Eq. (15), we only consider the case where the polynomial in the middle of this inequality is less than 3/2:

$$\Delta t \sum_{j \in \mathcal{N}_i} \left( \frac{d_0 (1 - \cos(k(j-i)))}{\|\mathbf{x}_j - \mathbf{x}_i\|^2} V_{ij} \right) + \Delta t \sum_{j \in \mathcal{N}_i} \left( \frac{v_j \cos(k(j-i))}{\|\mathbf{x}_j - \mathbf{x}_i\|} V_{ij} \right) \leq \Delta t \sum_{j \in \mathcal{N}_i} \left( \left( \frac{2d_0}{\|\mathbf{x}_j - \mathbf{x}_i\|^2} + \frac{|v_j|}{\|\mathbf{x}_j - \mathbf{x}_i\|} \right) V_{ij} \right) \leq \frac{3}{2} \quad (16)$$

From the second inequality in Eq. (15) and Eq. (16), we can derive the range of  $\Delta t$ :

$$\begin{cases} \Delta t \leq 0.75 \frac{1}{\sum_{j \in \mathcal{N}_i} \left( \left( \frac{d_0}{\|\mathbf{x}_j - \mathbf{x}_i\|} + 0.5 |v_j| \right) \frac{V_{ij}}{\|\mathbf{x}_j - \mathbf{x}_i\|} \right)} \\ \Delta t \leq 0.5 \frac{1}{\sum_{j \in \mathcal{N}_i} \left( \frac{|v_j|}{\|\mathbf{x}_j - \mathbf{x}_i\|} V_{ij} \right)} \end{cases} \quad (17)$$

To further simplify the time step condition, we subtract the two denominators in Eq. (17):

$$\sum_{j \in \mathcal{N}_i} \left( \left( \frac{\frac{4}{3}d_0}{\|\mathbf{x}_j - \mathbf{x}_i\|} + \frac{2}{3} |v_j| \right) \frac{V_{ij}}{\|\mathbf{x}_j - \mathbf{x}_i\|} \right) - \sum_{j \in \mathcal{N}_i} \left( \frac{2|v_j|}{\|\mathbf{x}_j - \mathbf{x}_i\|} V_{ij} \right) = \sum_{j \in \mathcal{N}_i} \left( \left( \frac{\frac{4}{3}d_0}{\|\mathbf{x}_j - \mathbf{x}_i\|} - \frac{4}{3} |v_j| \right) \frac{V_{ij}}{\|\mathbf{x}_j - \mathbf{x}_i\|} \right) \quad (18)$$

A sufficient condition for Eq. (18) to be less than zero is  $\frac{d_0}{\|\mathbf{x}_j - \mathbf{x}_i\|} - |v_j| \leq 0$ . Here, we assume that  $\frac{d_0}{\|\mathbf{x}_j - \mathbf{x}_i\|} - |v_j| \leq 0$ , under which Eq.(17) can be combined as:

$$\Delta t \leq 0.5 \frac{1}{\sum_{j \in \mathcal{N}_i} \left( \frac{|v_j|}{\|\mathbf{x}_j - \mathbf{x}_i\|} V_{ij} \right)} \quad (19)$$

Based on the conclusions drawn in [46,47], one can say that the numerical stability conditions for the central scheme are more stringent than those for the upwind/downwind scheme. Therefore, we apply Eq. (17) as the numerical stability conditions for the upwind/downwind schemes.

For the discretized versions of Eqs. (6) and (7), in order to ensure the stability of the time integrator, the time step is chosen according to the condition outlined in [51]. Therefore, the coupled model presented in this paper must satisfy the following stability conditions:

$$\left\{ \begin{array}{l} \Delta t \leq 0.25 \frac{\Delta x}{c} \\ \Delta t \leq 0.25 \left( \frac{\Delta x}{a} \right)^{\frac{1}{2}} \\ \Delta t \leq 0.125 \frac{\rho \Delta x^2}{\mu} \\ \Delta t \leq 0.5 \frac{1}{\sum_{j \in \mathcal{N}_i} \left( \frac{|v_j|}{\|\mathbf{x}_j - \mathbf{x}_i\|} V_{ij} \right)} \end{array} \right. \quad (20)$$

Next, we analyze the accuracy of the numerical method in this paper. First, for the time derivative, this paper uses the standard forward Euler method, for which the error is  $O(\Delta t)$ , meaning the temporal accuracy is first-order. For the analysis of spatial accuracy, we analyze the difference between the integral term in Eq. (1) and its corresponding discretized summation term. We first assume that  $D_1(\hat{\mathbf{x}} - \mathbf{x}) = \frac{1}{\|\hat{\mathbf{x}} - \mathbf{x}\|^2}$ ,  $D_2(\hat{\mathbf{x}} - \mathbf{x}) = \frac{1}{\|\hat{\mathbf{x}} - \mathbf{x}\|}$ , and  $M(\hat{\mathbf{x}}) = C(\hat{\mathbf{x}})v(\hat{\mathbf{x}})$ . The integral portion becomes:

$$\int_{\mathcal{H}_x} d_0(C(\hat{\mathbf{x}}) - C(\mathbf{x}))D_1(\hat{\mathbf{x}} - \mathbf{x})d\hat{\mathbf{x}} - \int_{\mathcal{H}_x} (M(\hat{\mathbf{x}}) - M(\mathbf{x}))D_2(\hat{\mathbf{x}} - \mathbf{x})d\hat{\mathbf{x}} \quad (21)$$

Since both terms have a similar structure, we will analyze the first term for brevity. This integral term can be written in the following form:

$$d_0 \int_A \int (C(\mathbf{x} + \xi) - C(\mathbf{x}))D(\xi)d\xi \quad (22)$$

where,  $\xi = (x, y)$  and  $A = \{(x, y) | x^2 + y^2 \leq \delta^2\}$ . We transform the above formula into the following formula without error:

$$d_0 \sum_{j \in \mathcal{N}_i} \int_B \int (C(\mathbf{x}_j + \xi) - C(\mathbf{x}_i))D(\mathbf{x}_j - \mathbf{x}_i + \xi)d\xi \quad (23)$$

where,  $B = \{(x, y) | \|x\| \leq \frac{\Delta x}{2}, |y| \leq \frac{\Delta x}{2}\}$ .

Assuming that the functions  $C$  and  $D$  are twice continuously differentiable, we can apply a Taylor series expansion around the center of node  $j$  and the displacement vector  $\mathbf{x}_j - \mathbf{x}_i$  respectively:

$$C(\mathbf{x}_j + \xi) = C(\mathbf{x}_j) + \nabla C(\mathbf{x}_j) \cdot \xi + O(|\xi|^2) \quad (24)$$

$$D(\mathbf{x}_j - \mathbf{x}_i + \xi) = D(\mathbf{x}_j - \mathbf{x}_i) + \nabla D(\mathbf{x}_j - \mathbf{x}_i) \cdot \xi + O(|\xi|^2) \quad (25)$$

Substituting these expansions into Eq. (23) and integrating over the symmetric domain  $A$  causes the odd-powered terms in  $\xi$  to integrate to zero. This leads to the following expression:

$$d_0 \sum_{\substack{j \in \mathcal{N}_i \\ j \neq i}} [(C(\mathbf{x}_j) - C(\mathbf{x}_i))D(\mathbf{x}_j - \mathbf{x}_i)\Delta x^2 + O(\Delta x^4)] = d_0 \sum_{\substack{j \in \mathcal{N}_i \\ j \neq i}} [(C(\mathbf{x}_j) - C(\mathbf{x}_i))D(\mathbf{x}_j - \mathbf{x}_i)\Delta x^2] + O(\Delta x^2) \quad (26)$$

It should be noted that while the truncation error for a single node is  $O(\Delta x^4)$ , the total truncation error, when summed over all nodes within the two-dimensional horizon, becomes  $O(\Delta x^2)$ . This conclusion is consistent with Ref. [68].

For the reaction term, to prevent the unphysical result of reactant concentrations dropping below zero within a single time step—an issue that arises from high reaction rates and introduces numerical errors—we adopt the same method as used in [47]:  $\Delta t \sum_{q=1}^{M_p} R_{pq}(\mathbf{x}_i, t) \leq C_p(\mathbf{x}_i, t)$ .

### 3.2. Boundary conditions

Various methods for applying local boundary conditions in PD models have been explored in [69–71]. In this paper, the local boundary conditions are imposed using the fictitious nodes method (FNM) [69,70,72,73]. FNM involves adding an outer boundary layer with a thickness equal to the radius of the horizon at the boundary. This method is relatively simple, easy to implement, and naturally applicable to a wide range of complex boundaries. Therefore, the FNM method is employed in this study.

For imposing the no-slip solid wall boundary condition, we use the same naïve-type FNM [73] as in [51] to set  $v_x^{\text{wall}} = v_y^{\text{wall}} = 0$ . However, the no-slip solid wall boundary condition proposed in [51] does not strictly enforce the  $\mathbf{v} \cdot \mathbf{n} = 0$  condition in complex flow situations, so this boundary condition is modified here. We initialize the density of virtual nodes with  $\rho_0$ , treating them as fluid nodes whose density evolves naturally over time. By doing so, the density of the virtual wall nodes increases when the node velocity is directed towards the wall. According to the equation of state (Eq. (5)), as the density increases, the pressure also increases, generating an outward resistance that reduces the velocity directed towards the wall. Thus, the impermeability condition of the rigid wall ( $\mathbf{v} \cdot \mathbf{n} = 0$ ) is implicitly enforced (see Appendix D for a comparison of solid wall boundary conditions).

For the velocity inlet boundary conditions, the velocities of the virtual nodes are uniformly set to a fixed value  $v_0$ . The pressures of these virtual nodes are assigned the values of the corresponding mirror nodes, as shown in Fig. 3. For the pressure outlet boundary conditions, the pressure of the virtual nodes at the outlet is uniformly set to 0. Since the pressure outlet boundary conditions discussed in this paper assume normal-phase flows, it is necessary to specify that the velocity in the y-direction is 0. It is worth noting that the treatment of boundary conditions may vary with different node distributions [74].

In contrast to the work in [46,47], we propose a model that can simulate the ARD problem under a non-uniform flow field within a nonlocal framework by coupling the governing equations of PD for viscous flow with the PD-ARD model for non-uniform flow. Additionally, we introduce a density diffusive term to the PD mass conservation equation (Eq. (3)) to mitigate numerical oscillations. Further, we propose multiple methods for applying boundary conditions. In the subsequent section, we introduce the PD equations for bimolecular reactions and solid dissolution (Eqs. (28) and (29)). Fig. 4 and Appendix E illustrates the computational workflow when these equations are coupled with the PD viscous flow model, under specific boundary and initial conditions. The PD-ARD framework presented herein comprises two main components: a “Viscous Flow Main Solver” and a “Dissolution/Bimolecular Reaction Main Solver”. The Viscous Flow solver calculates the steady-state flow field using the central scheme. The Dissolution/Bimolecular Reaction solver utilizes a hybrid scheme. The flow field is considered to have reached a steady state when the change in nodal velocities between consecutive time steps, computed by the formula below, is smaller than  $5 \times 10^{-6}$ :

$$\varepsilon = \sqrt{\frac{\sum_{i=1}^N (v_i^{n+1} - v_i^n)^2}{\sum_{i=1}^N (v_i^n)^2}} \quad (27)$$

where,  $N$  represents the total number of nodes in the computational domain.

In most instances, there is a separation between the relevant physical time-scales of the dissolution/reaction and fluid motion phenomena. This warrants adoption of a “weak coupling” between the two solvers shown in Fig. 4. When the time step required by the fluid flow solver is much smaller than that of the dissolution solver, the steady-state flow field is computed first, on the faster time-

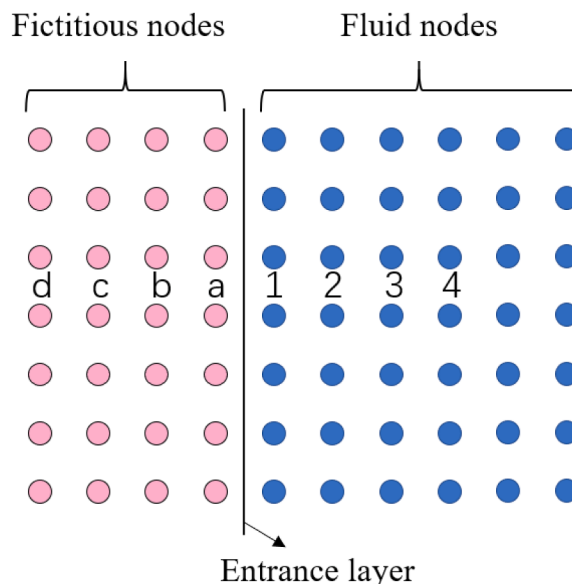


**Fig. 3.** Velocity inlet boundary conditions.

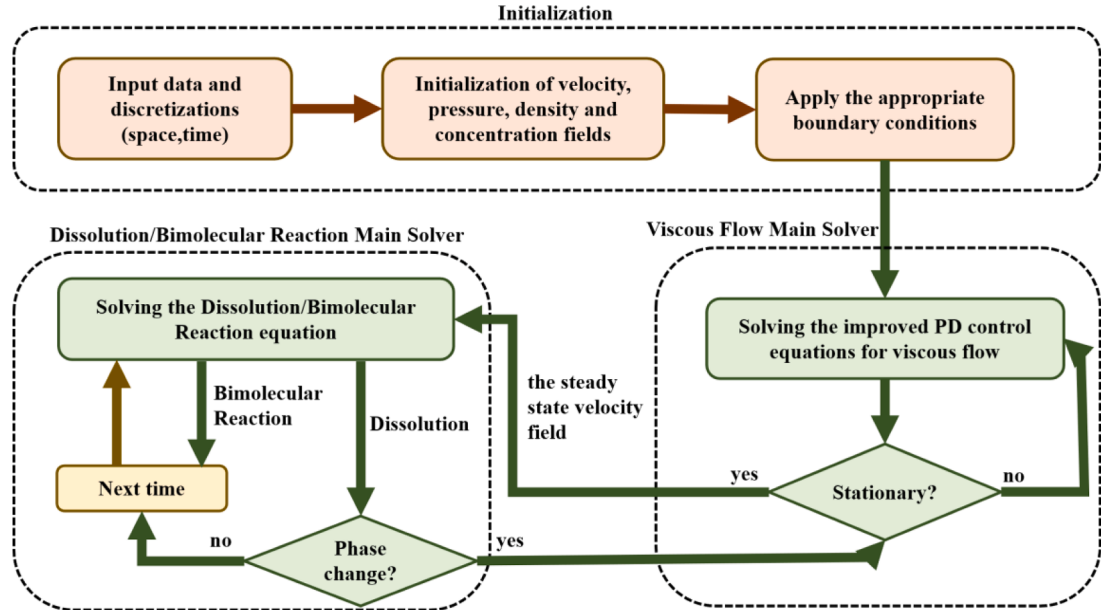


**Fig. 4.** Flowchart illustrating the calculation process of the PD-ARD model in bimolecular reactions or solid dissolution.

scale, because the amount of solid dissolution is negligible during the short time it takes for the flow field to reach a steady state. This method can effectively reduce computational costs while ensuring accuracy. When the two processes happen on the same time scale, then a single time-step needs to be used and both models are solved at each time step. In the example of Fig. 5(a), the flow field solver requires approximately 2.3 times more computational time than the bimolecular reaction solver to compute an equal number of time steps.

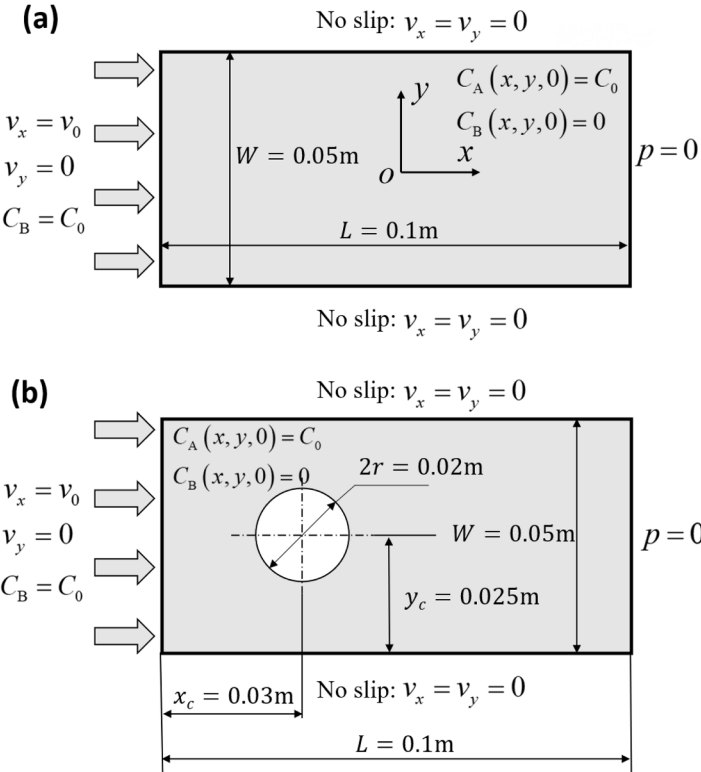


**Fig. 5.** Boundary and initial conditions for numerical verification examples.

#### 4. Numerical examples and analysis

In this section, ARD problems flow in a simple channel and flow around a cylinder in a channel are first used in [Section 4.1](#) to test and verify the new model formulation, including the boundary conditions. In [Section 4.2](#), the present model is applied to the ARD problem in inhomogeneous media and compared with the results in [\[47\]](#). Additionally, this model is used to study the effect of different Reynolds numbers on the dissolution of solids.

##### 4.1. Model verification

We consider an irreversible bimolecular reaction involving three substances:  $A + B \rightarrow AB$ . All substances are assumed to be water-soluble. For the purposes of this analysis, we assume that the diffusion coefficients for each substance are equal, with a value of  $D = 0.0017 \text{ cm}^2/\text{s}$  for the irreversible bimolecular case. Consequently, [Eq. \(1\)](#) can be rewritten accordingly:

$$\left\{ \begin{array}{l} \frac{\partial C_A(\mathbf{x}, t)}{\partial t} = \int_{\mathcal{X}} d_0 \frac{\hat{C}_A - C_A}{\|\hat{\mathbf{x}} - \mathbf{x}\|^2} d\hat{\mathbf{x}} - \int_{\mathcal{X}} \frac{\hat{C}_A \hat{v} - C_A v}{\|\hat{\mathbf{x}} - \mathbf{x}\|} d\hat{\mathbf{x}} - R_{AB} C_A C_B \\ \frac{\partial C_B(\mathbf{x}, t)}{\partial t} = \int_{\mathcal{X}} d_0 \frac{\hat{C}_B - C_B}{\|\hat{\mathbf{x}} - \mathbf{x}\|^2} d\hat{\mathbf{x}} - \int_{\mathcal{X}} \frac{\hat{C}_B \hat{v} - C_B v}{\|\hat{\mathbf{x}} - \mathbf{x}\|} d\hat{\mathbf{x}} - R_{AB} C_A C_B \\ \frac{\partial C_{AB}(\mathbf{x}, t)}{\partial t} = \int_{\mathcal{X}} d_0 \frac{\hat{C}_{AB} - C_{AB}}{\|\hat{\mathbf{x}} - \mathbf{x}\|^2} d\hat{\mathbf{x}} - \int_{\mathcal{X}} \frac{\hat{C}_{AB} \hat{v} - C_{AB} v}{\|\hat{\mathbf{x}} - \mathbf{x}\|} d\hat{\mathbf{x}} + R_{AB} C_A C_B \end{array} \right. \quad (28)$$

where,  $C_A, C_B$  and  $C_{AB}$  represent the concentrations of substances A, B and AB, respectively. The reaction rate for the bimolecular reaction, denoted by  $R_{AB}$ , is set to  $R_{AB} = 4.1 \text{ L}/(\text{mol} \cdot \text{s})$  for all bimolecular reactions discussed in this paper.

In this section, two-dimensional ARD problems are considered, as illustrated in [Fig. 5](#). Specifically, [Fig. 5\(a\)](#) depicts the ARD problem in a simple domain, used to test the inlet and outlet boundary conditions. Meanwhile, [Fig. 5\(b\)](#) illustrates the ARD problem in the flow around a cylinder, utilized to test the no-slip surface boundary conditions. These examples serve to validate the proposed coupled PD-ARD model by comparing the solutions, in the limit of the horizon going to zero, with the corresponding ones for the classical model. The fluid has a density of  $\rho = 1000 \text{ kg/m}^3$  and a viscosity of  $\mu = 10^{-3} \text{ kg} \cdot \text{m}^{-1}$  values that apply consistently throughout the paper. Additionally, the artificial speed of sound is set to  $c_0 = 0.01 \text{ m/s}$ . The inlet velocity is defined as  $v_0 = 1 \times 10^{-4} \text{ m/s}$ , with an initial concentration of  $C_0 = 0.02 \text{ mol/L}$ , and the outlet is maintained at zero pressure. The specific boundary conditions applied are detailed in [Section 3.2](#).

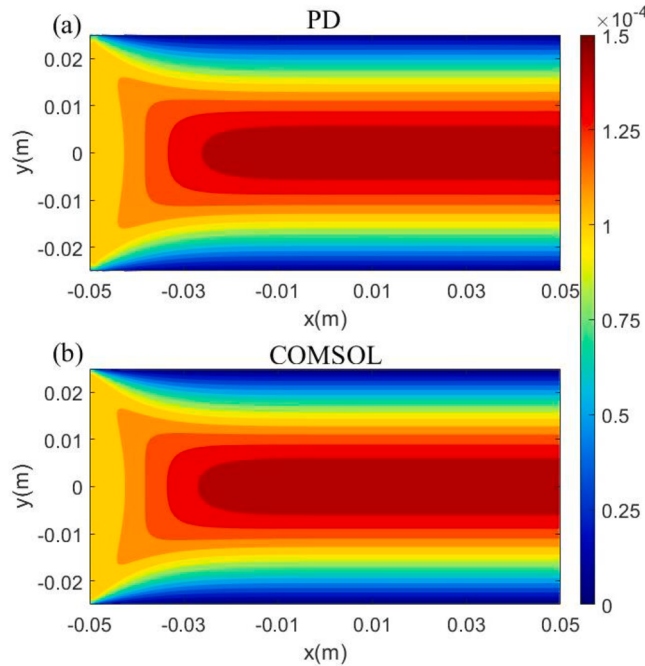


**Fig. 6.** Velocity plots of the PD solution and the COMSOL solution in the x-direction for the homogeneous medium arithmetic example. (a) represents the PD solution with a horizon of 2 mm, and (b) represents the COMSOL solution for the corresponding classical model.

For the example in Fig. 5(a), we use a horizon size  $\delta = 2$  mm. To maintain a relative grid-density  $m$  ( $m$  the ratio between the horizon size and grid spacing) of 4, the domain is uniformly discretized with a grid spacing of  $\Delta x = L/200$ . The PD solution converges to the classical solution as the horizon size  $\delta$  approaches zero, while keeping  $m$  constant. This is referred to as  $\delta$ -convergence [75] (see Appendix F for a convergence study). The time step used for solving the flow field component is  $\Delta t_v = 0.01$  s, while the time step for the substance transfer and reaction component is  $\Delta t_R = 0.01$  s. For the example depicted in Fig. 5(b), we use a horizon size  $\delta = 1$  mm and  $m = 4$ , yielding  $\Delta x = L/400$ . The time step for solving the flow field part is  $\Delta t_v = 5 \times 10^{-3}$  s, and the time step for the substance transfer and reaction part remains  $\Delta t_R = 0.01$  s.

The corresponding classical model was solved using the finite element method in COMSOL Multiphysics® v6.0. A two-step approach was employed: a stationary study for the steady-state flow field, followed by a transient study for species transport and reaction. For spatial discretization, the mesh was generated using the “Finer” predefined size setting. First-order elements were used for flow and transport, while second-order elements were applied to chemistry. The model utilized an adaptive Backward Differentiation Formula (BDF) transient solver with a maximum order of 2 and a relative tolerance of 0.005, employing the Parallel Direct Sparse Solver (PARDISO) for the linear system.

Fig. 6 and Fig. 7 show the converged results of the velocity field obtained using the improved PD governing equations for viscous flow and COMSOL simulations of the corresponding classical model. The results demonstrate that the velocity field predicted by the PD model aligns well with the velocity field obtained by COMSOL. This result verifies the proposed velocity inlet, pressure outlet, and no-slip solid wall boundary conditions, and checks the accuracy of the improved PD control equations for viscous flow. In some cases, the solution obtained from the PD model can even be more stable than the solution from COMSOL (see Fig. 8(b)).

The comparison of the time evolution for the concentration of the product AB shown in Fig. 9 and Fig. 11, confirms that the results from the PD model are in good agreement with those from COMSOL. We also compare the concentrations of substances A, B and AB from the PD model and the COSMOL solution for the corresponding classical model along the horizontal line  $y = 0$  (see Fig. 10) in the example with the domain without obstacles, shown in Fig. 5(a). Additionally, we compare the concentrations of AB from the PD model and the COSMOL solution for the corresponding classical model along the horizontal line  $y = 0.015$  m (see Fig. 12) in the example of flow around a cylinder, shown in Fig. 5(b), at different times. The horizon size used in these plots was sufficiently small to allow the coupled PD-ARD model match closely the COMSOL outputs of the classical model.

## 4.2. Applications to advection-reaction-diffusion problems

### 4.2.1. Flow and reactions in a channel with multiple obstacles

Most ARD processes occur in complex domains that may also change in time, for instance when the reactions dissolve one of the solid constituents. In groundwater contamination remediation, the injected remediation agent flows alongside the groundwater and undergoes chemical reactions with contaminants. The flow is significantly influenced by the permeable or impermeable rocks. Atmospheric pollutants like sulfur dioxide and nitrogen oxides are transported through air currents and may chemically react (e.g., photochemically) with other substances. Buildings or natural relief features can also influence this ARD process.

As illustrated in Fig. 13, the simplifying assumption of uniform velocities throughout the entire domain is utilized for similar flow field problems in the literature [47]. However, this method overlooks the fact that flow in such a channel is strongly influenced by

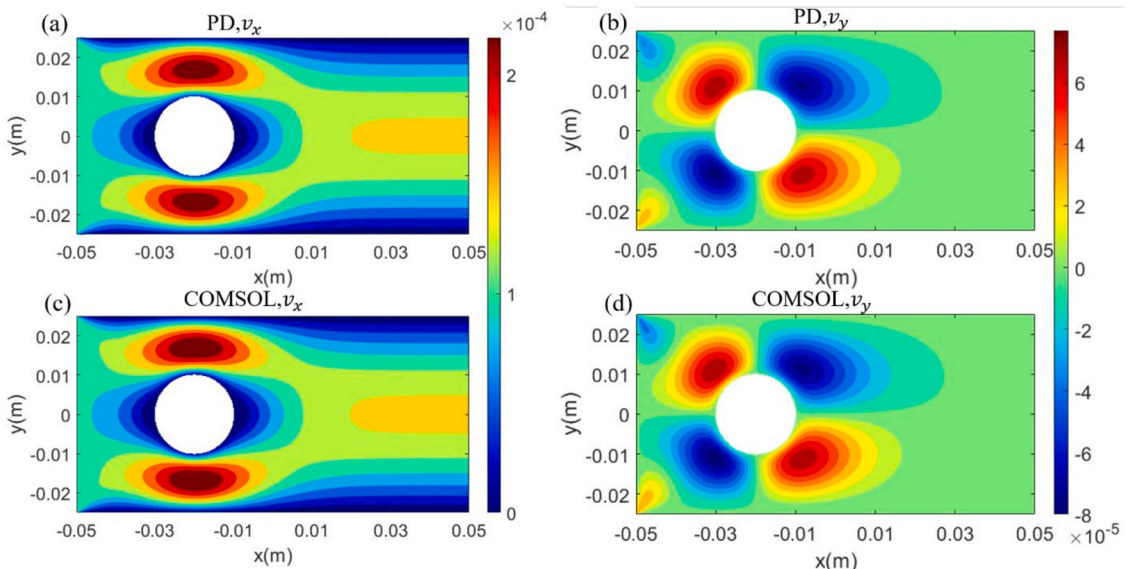


**Fig. 7.** Velocity comparison between the PD solution and the COMSOL solution in the example of flow around a cylinder. Subfigures (a) and (b) represents the PD solution with a horizon of 2 mm. Subfigures (c) and (d) represents the COMSOL solution for the corresponding classical model.

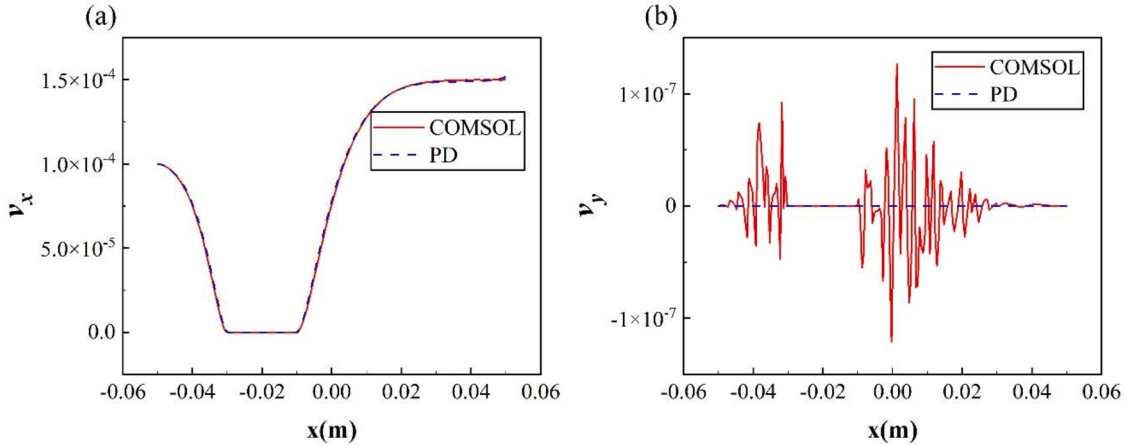


**Fig. 8.** Comparison of velocities between the PD solution and the COMSOL solution along the horizontal line  $y = 0$  for the example of flow around a cylinder, where (a) represents the velocity in the  $x$ -direction and (b) represents the velocity in the  $y$ -direction.

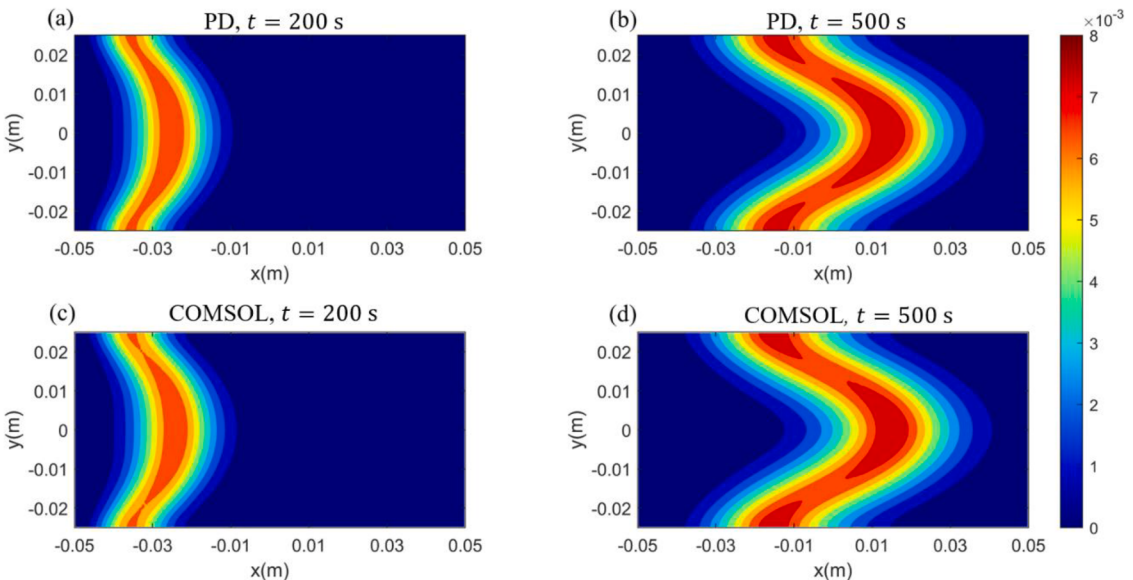


**Fig. 9.** Comparison plots of the concentrations of the product AB obtained by the PD-ARD model with a horizon of 2 mm and COMSOL solving the corresponding classical model in a homogeneous domain.

obstacles, and that influences the material transport and reaction/diffusion processes.

Fig. 13 adopts a boundary condition with a fixed inlet velocity of  $v_0 = 0.0121$  cm/s and a zero-pressure outlet condition. Additionally, an artificial sound velocity of  $c_0 = 0.01$  m/s is employed. This configuration better reflects the flow characteristics of fluids in domains with complex geometries. Here, we use a horizon size  $\delta = 6$  mm and  $m = 4$ , yielding  $\Delta x = L/200$ . The time step for computing the flow velocity is  $\Delta t_v = 0.1$  s, while the time step for the material transfer and reaction computation is  $\Delta t_R = 0.1$  s.

Through numerical simulation, we obtain the steady-state flow velocity distribution, as shown in Fig. 14. To analyze the impact of non-uniform flow velocities on material transport, we simulate the ARD process, recording the product AB concentration distribution at 1000 s (see Fig. 15(a)). This is compared to the assumption of uniform flow velocities in the literature [47] (see Fig. 15(b)).

The differences between using the actual velocity field compared with an assumed uniform one are significant, indicating the need to for simulating the complex ARD conditions in complex domains.

#### 4.2.2. Dissolution of solids in fluid flow under ARD conditions

In the preceding section we have demonstrated the applicability of the proposed PD-ARD model to ARD processes. By modifying the

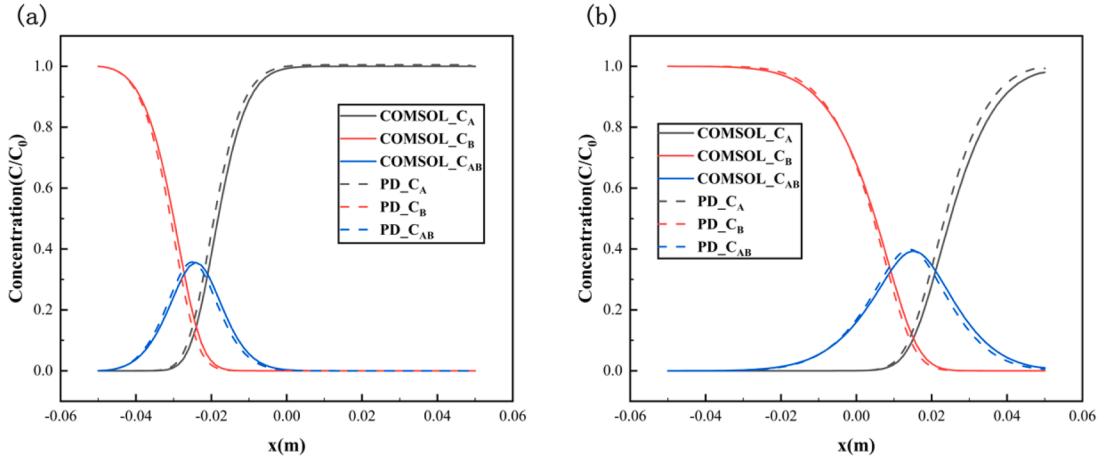


**Fig. 10.** Comparison of concentrations of each substance obtained by PD and COMSOL at 200 s (a) and 500 s (b) along the horizontal line  $y = 0$  for the ARD example in the domain without an obstacle.

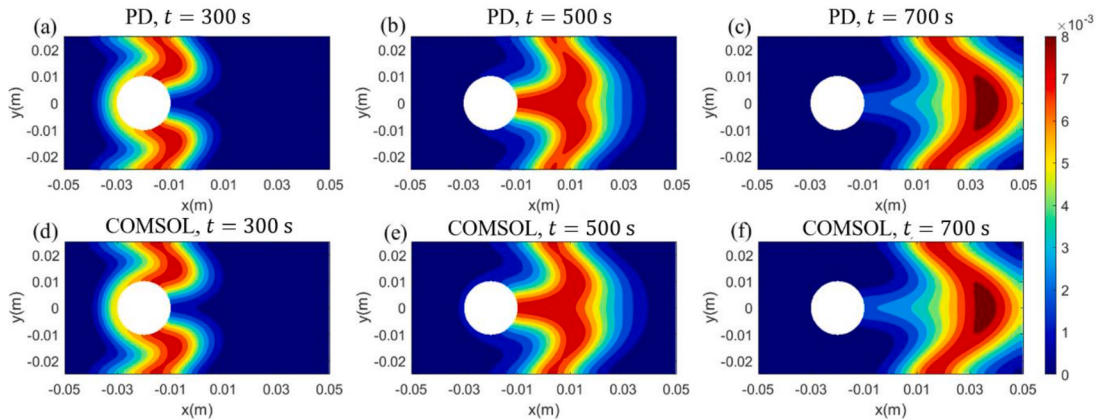


**Fig. 11.** Comparison plots of the concentrations of the product AB obtained by the PD-ARD model with a horizon of 1 mm and COMSOL solving the corresponding classical model for the flow around a cylinder.

reaction terms appropriately, our model can be extended to encompass dissolution-convection-diffusion processes. Investigating these processes may lead to, for example, simulation of karst formation and other geotechnical applications, optimization of drug solubility, enhancing absorption efficiency and other biomedical applications. Furthermore, the model has applications in food processing and preservation, where dissolution conditions influence taste, color, and nutrient content. In this section, we utilize the PD-ARD model to investigate solid dissolution and assess how different Reynolds numbers affect the dissolution process.

Consider the example presented in Fig. 5(b), where the cylindrical obstacle, representing substance A, is now assumed to be soluble, and the dissolved substance in water is the product AB. This dissolution process is modeled as an irreversible chemical reaction:  $A \rightarrow AB$ . The PD-ARD equations governing this process are as follows:

$$\begin{cases} \frac{\partial C_A(\mathbf{x}, t)}{\partial t} = -R_A \\ \frac{\partial C_{AB}(\mathbf{x}, t)}{\partial t} = \int_{\mathcal{H}_x} d_0 \frac{C_{AB}(\hat{\mathbf{x}}, t) - C_{AB}(\mathbf{x}, t)}{\|\hat{\mathbf{x}} - \mathbf{x}\|^2} d\hat{\mathbf{x}} - \int_{\mathcal{H}_x} \frac{C_{AB}(\hat{\mathbf{x}}, t)v(\hat{\mathbf{x}}, t) - C_{AB}(\mathbf{x}, t)v(\mathbf{x}, t)}{\|\hat{\mathbf{x}} - \mathbf{x}\|} d\hat{\mathbf{x}} + R_A \end{cases} \quad (29)$$

where,  $R_A$  denotes the dissolution rate of substance A in solution. In this paper, we assume that the dissolution rate remains constant at  $R_A = 4.2 \text{ mol}/(\text{L} \cdot \text{s})$ . The concentration of the solid phase of substance A is given as  $C_{A,\text{solid}} = 100 \text{ mol/L}$ . It is assumed that the saturation concentration of AB is  $C_{\text{sat}} = 20 \text{ mol/L}$ . During the solid dissolution process, dissolution ceases once the concentration of AB reaches saturation. When the concentration of AB falls below the saturation level, the dissolution resumes.

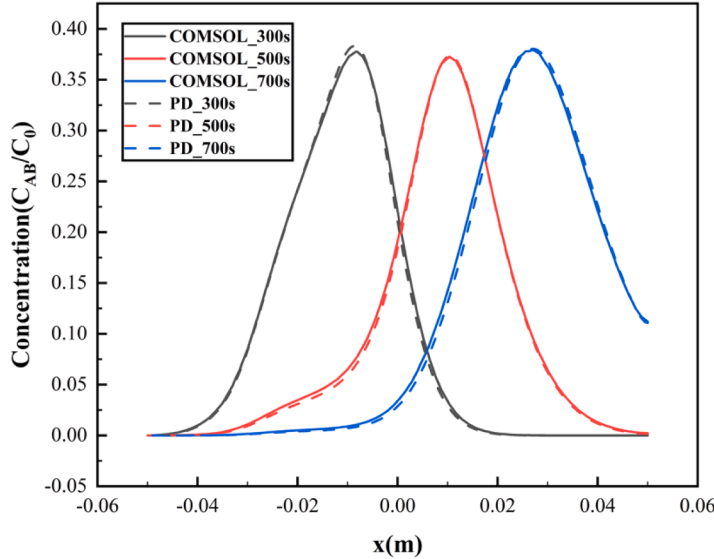


**Fig. 12.** Comparison of concentrations of the substance AB obtained by PD and COMSOL along the horizontal line  $y = 0.015$  m at different times for the ARD example of flow around a cylinder.

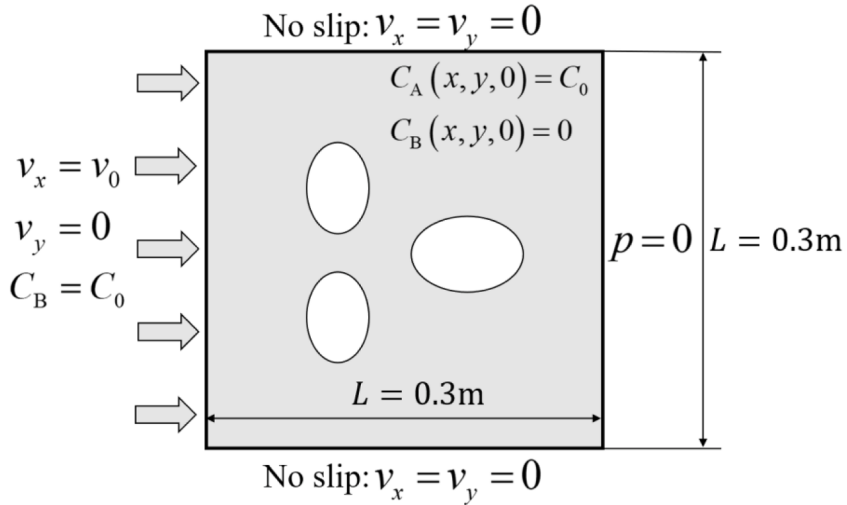


**Fig. 13.** Setup for an ARD problem in a domain with three ovoid obstacles (e.g., stones).

The diffusion rate of substance AB in the solution is set to  $D = 1 \times 10^{-6}$  m<sup>2</sup>/s. This example uses the same configuration as Fig. 5 (b), with the only modifications being the solubility of the obstacle and a different inlet velocity. Three flow cases are considered with inlet velocities  $v_0 = 1 \times 10^{-4}$  m/s,  $5 \times 10^{-4}$  m/s,  $25 \times 10^{-4}$  m/s, corresponding to Reynolds numbers  $Re = 2, 10, 50$ , respectively. The associated artificial sound speeds for these cases are  $c_0 = 0.01$  m/s,  $0.05$  m/s,  $0.25$  m/s. The time steps used for solving the flow field component are  $\Delta t_v = 0.01$  s,  $0.001$  s,  $0.0001$  s, respectively, while the time steps for solid dissolution are  $\Delta t_R = 0.01$  s,  $0.1$  s,  $0.1$  s, respectively.

The evolution of the dissolution of substance A for the three different Reynolds numbers is shown in Fig. 16 (see also Videos S1-S3). Interestingly, increasing the Reynolds number value not only accelerates the dissolution rate of the cylinder but amplifies the asymmetry of the yet to be dissolved solid. The higher Reynolds number enhances fluid scouring effects on the upstream side, as well as the flow-parallel sides of the obstacle, resulting in a faster dissolution rate in these regions. In Fig. 17, we show the concentration of the dissolved substance, dissolution product AB (substance A in liquid phase), for different Reynolds number values. This left-right asymmetry can be quantified by computing the sum of the particles of the solid, but dissolvable, substance A on both sides of the

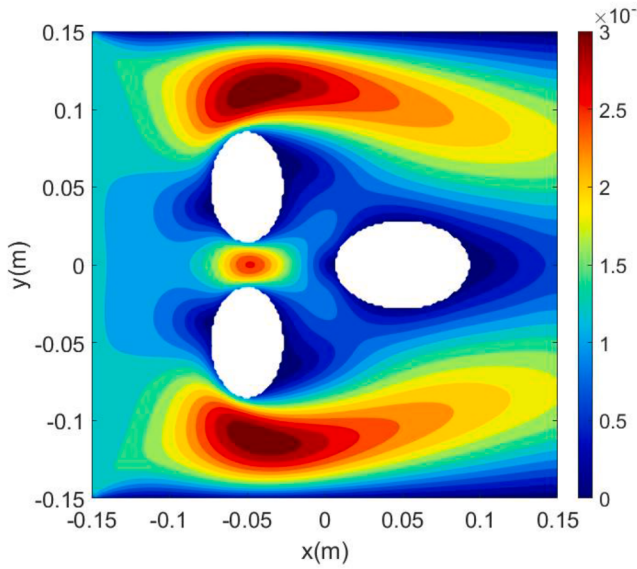


**Fig. 14.** Flow velocity magnitude for the PD solution in the domain with three obstacles.

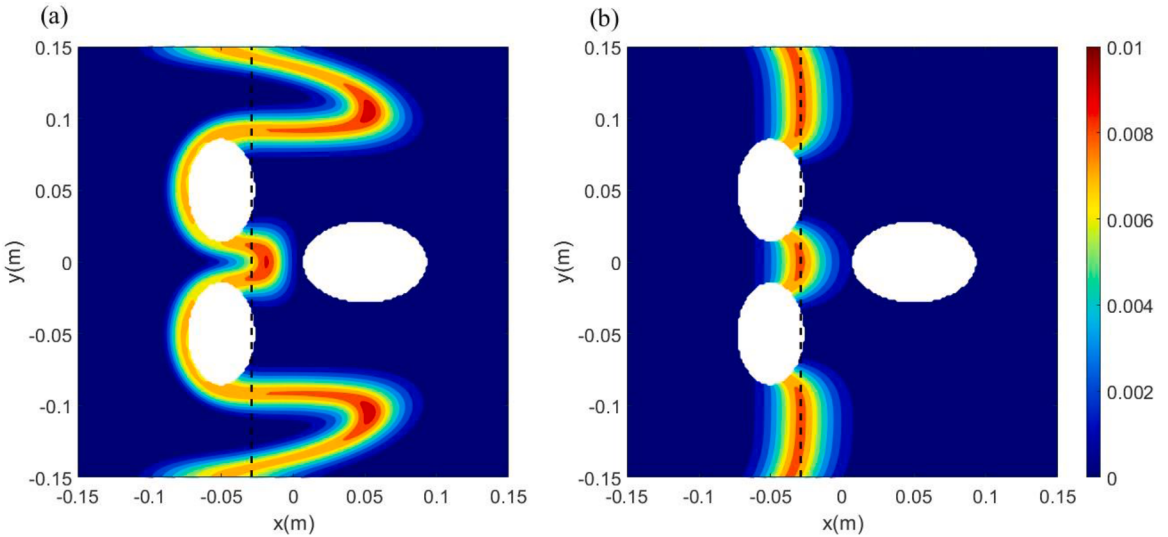


**Fig. 15.** Concentration of AB product at 1000 s using (a) the computed, non-uniform flow field, and (b) using the imposed uniform flow field described in [47]. The black dotted line in the graph indicates the position  $x = -0.029$  m (starting at  $x = -0.15$  m, the flow has  $v_0 = 0.0121$  cm/s, which means that the concentration peaks under the constant flow velocity through the domain reaches  $x = -0.029$  m after a time of 1000 s).

cylinder (see Fig. 18), as described by the following equation:  $N_{\text{total}/2} = \sum_{i=1}^n C_A(i, 0) \Delta x^2 / 2$  represents half of the remaining solid substance A in the initial dissolvable disk, and  $n$  denotes the total number of nodes used to discretize the entire domain of the problem. Furthermore, the quantities  $N_A^{\text{downwind}} = \sum_{i=1}^{\text{downwind}} \Delta x^2 C_A^{\text{downwind}}(i, t)$  and  $N_A^{\text{upwind}} = \sum_{i=1}^{\text{upwind}} \Delta x^2 C_A^{\text{upwind}}(i, t)$  represent the sums of the remaining particles of substance A on the upwind and downwind halves of the cylinder, respectively, at time  $t$ .

A further analysis of Fig. 17 and Fig. 18, confirm that early in the dissolution process, the dissolution rates upwind and downwind are nearly identical. This is because diffusion primarily influences the dissolution rate at this stage, and the diffusion rate remains consistent across all three conditions. However, as the dissolution process progresses, substance AB flows left to right, causing the downstream region to reach the saturation concentration of AB more easily than the upstream region. Consequently, at a given Reynolds number, the dissolution rate on the upwind side of the dissolvable obstacle consistently exceeds that on the right side. It is noteworthy that this asymmetric dissolution behavior between upwind and downwind regions has also been observed in [76]. As the Reynolds number increases, the residence time of substance AB on the upwind side decreases, making it less likely to reach the saturation concentration, which makes the asymmetry more pronounced.

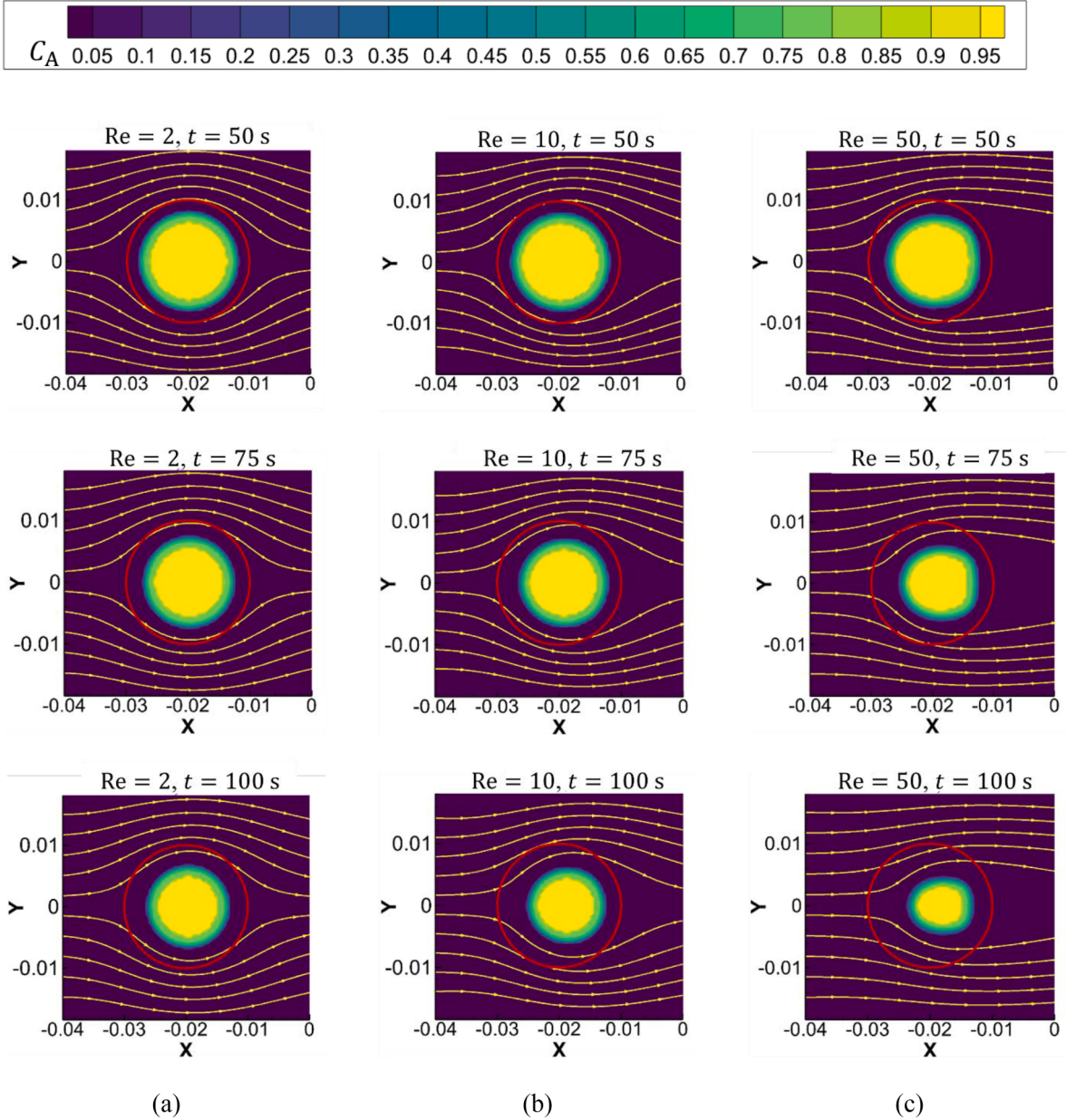


**Fig. 16.** The time-evolution for the concentration of the solid phase in the dissolution problem for different Reynolds numbers: (a)  $Re = 2$ , (b)  $Re = 10$ , and (c)  $Re = 50$ . The flow streamlines, at each of the times shown, as well as the contour of the original size of the solid in the flow, are superposed onto the plots.

## 5. Conclusions

This paper presents a robust peridynamic (PD) framework for modeling Advection-Reaction-Diffusion (ARD) processes under non-uniform flow conditions, addressing key limitations of classical approaches. Classical models, which are based on partial differential equations (PDEs), encounter fundamental difficulties when dealing with physical discontinuities (e.g., fractures, material interfaces) and non-local interactions inherent in many systems. The PD-ARD equations for non-uniform flow are derived from the general PD continuity equation in the Eulerian framework, along with the PD-ARD equation for uniform flow. To ensure numerical stability and accuracy, we introduce enhancements to the PD equations under viscous flow, effectively reducing numerical oscillations, and refine

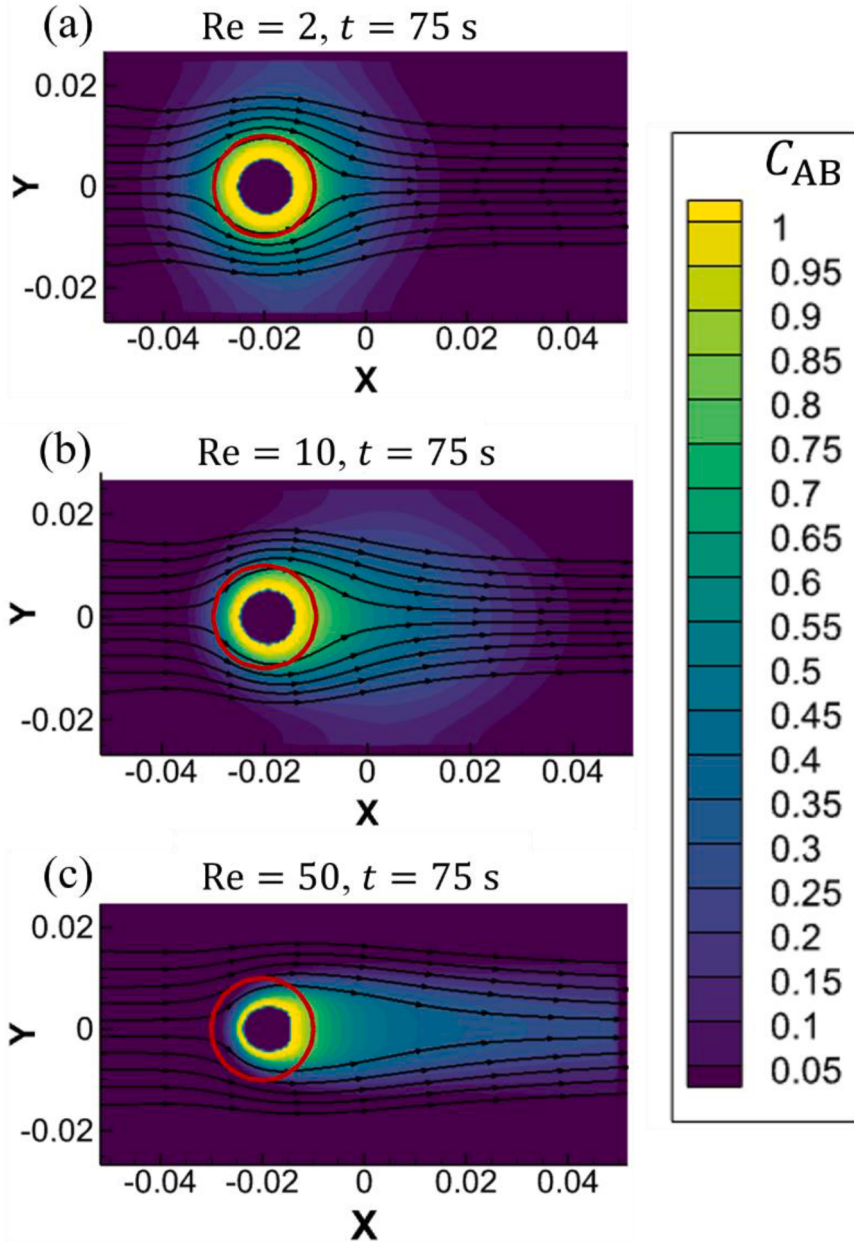


**Fig. 17.** The concentration distribution of the dissolution product AB at 75 s for different Reynolds numbers (where  $C_{AB}$  represents the concentration of node AB normalized by the saturation concentration of AB). The flow streamlines, for each of the  $Re$  values shown, as well as the contour of the original size of the dissolvable solid in the flow, are superposed onto the plots.

the boundary conditions to achieve higher precision. The PD-ARD model for viscous flow is constructed by coupling the improved PD equations for viscous flow with the PD-ARD equations for non-uniform flow, offering a unified and nonlocal framework for complex ARD simulations.

The new nonlocal model and boundary conditions are validated by simulating ARD problems of 2D flow in a simple channel and around a cylinder, and comparing the PD results with those from COMSOL obtained for the corresponding classical problem. The model is then applied to ARD problems in domains with multiple obstacles and is also used to study the effect of different Reynolds numbers on the dissolution of a solid in a fluid flow. The flow-accelerated boundary shift or phase transition in the model occurs autonomously, without requiring modifications to the predefined material solid/fluid interface.

The proposed framework not only advances the modeling of ARD processes under non-uniform flow but also opens new avenues for

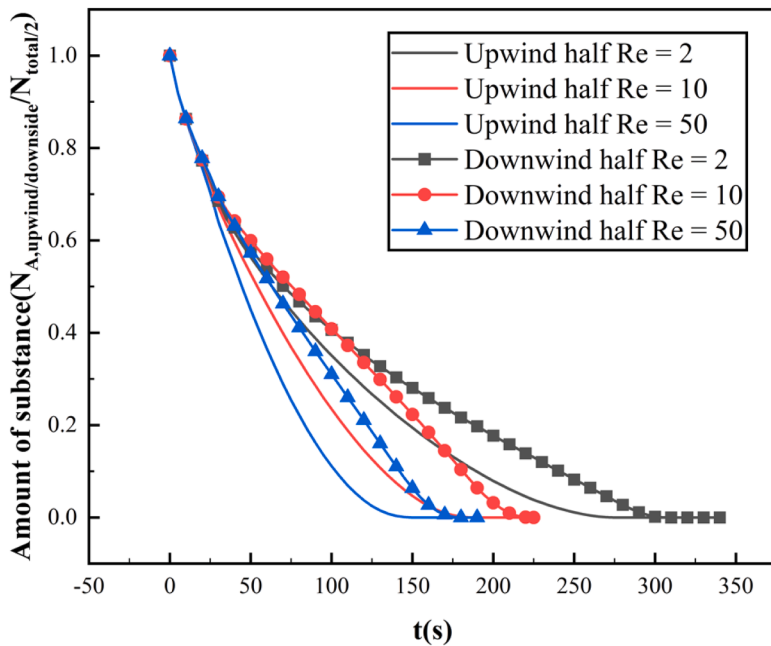


**Fig. 18.** The asymmetry of dissolution in flow: comparison between the remaining solid substance in the initial dissolvable disk relative to the symmetry line upwind (“left”) and downwind (“right”) sides of the disk, at different Reynolds numbers.

exploring a wide range of applications. These include, but are not limited to, corrosion processes, karst formation, ice melting dynamics, ablation, and the charging and discharging mechanisms of lithium-ion batteries. Future work will focus on extending the model to three-dimensional domains and incorporating additional physical phenomena to further broaden its applicability.

#### CRediT authorship contribution statement

**Zhaoyang Song:** Writing – original draft, Writing – review & editing, Validation, Visualization, Software. **Chenwen Tian:** Writing – review & editing, Software. **Juan Du:** Writing – review & editing, Project administration. **Florin Boarbu:** Writing – review & editing. **Ziguang Chen:** Writing – review & editing, Conceptualization, Supervision, Funding acquisition.

#### Declaration of competing interest

The authors declare that they have no known competing financial interests or personal relationships that could have appeared to influence the work reported in this paper.

#### Acknowledgments

This work was supported by the National Natural Science Foundation of China (No. 12372208), the Fundamental Research Funds for the Central Universities (No. 2021GCRC021). The work of F.B was supported in part by the National Science Foundation under CMMI CDS&E award No. 1953346.

#### Supplementary materials

Supplementary material associated with this article can be found, in the online version, at [doi:10.1016/j.cma.2025.118311](https://doi.org/10.1016/j.cma.2025.118311).

#### Appendix A. Numerical oscillations

The analysis corresponds to the example depicted in Fig. 5(b) of Section 4.1. Here, we set the  $\delta = 1$  mm and  $m = 4$ . The time step used for solving the flow velocity component is  $\Delta t_v = 5 \times 10^{-3}$  s. Fig. 19 presents a comparison of the results with and without the inclusion of the density diffusive term.

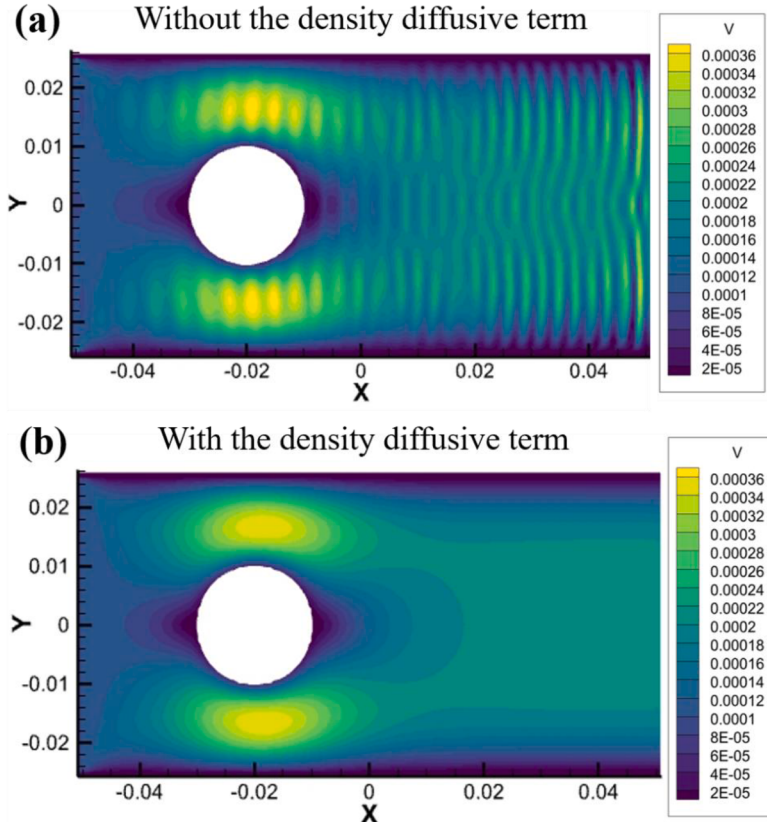


Fig. 19. Comparison of results after calculating  $6000\Delta t_v$ .

## Appendix B. Stability Analysis of the Downwind Scheme for the Convection Equation

The one-dimensional constant advection equation in the PD framework can be written as:

$$\frac{\partial \rho(\mathbf{x}, t)}{\partial t} = - \int_{\tilde{\mathcal{H}}_x} \frac{\hat{\rho} - \rho}{\|\hat{\mathbf{x}} - \mathbf{x}\|} v d\hat{\mathbf{x}} \quad (30)$$

where  $v = \frac{a}{V_{\mathbf{x}}} \mathbf{v} \cdot \mathbf{e}(\mathbf{x}, \hat{\mathbf{x}})$ . Here, we use midpoint integration to approximate the integral term and a forward Euler method for the time discretization. The discretized equation is then the following:

$$\rho_i^{n+1} = \rho_i^n + \Delta t \left[ - \sum_{\substack{j \in \tilde{\mathcal{H}}_i \\ j \neq i}} \left( \frac{\rho_j^n - \rho_i^n}{\xi_{ij}} v_i^n V_{ij} \right) \right] \quad (31)$$

where,  $\tilde{\mathcal{H}}_i$  represents the down-wind portion of the horizon. Applying von Neumann stability analysis, we use the following form for the error term:

$$\epsilon_j^n = \epsilon^n e^{kj\sqrt{-1}} \quad (32)$$

Substituting this into Eq. (31) yields the amplification factor:

$$\|\varepsilon\| = \left\| 1 - \Delta t \sum_{\substack{j \in \mathcal{N}_i \\ j \neq i}} \left( \frac{e^{k(j-i)\sqrt{-1}} v_i - v_i V_{ij}}{\|x_j - x_i\|} \right) \right\| \quad (33)$$

By substituting Euler's formula  $e^{wx\sqrt{-1}} = \cos wx + \sqrt{-1}\sin wx$ , into the equation above, we get:

$$\|\varepsilon\| = \left\| 1 + \Delta t \sum_{\substack{j \in \mathcal{N}_i \\ j \neq i}} \left( \frac{(1 - \cos k(j-i)) v_i}{\|x_j - x_i\|} V_{ij} \right) - \Delta t \sum_{j \in \mathcal{N}_i} \left( \frac{\sqrt{-1} \sin k(j-i) v_i}{\|x_j - x_i\|} V_{ij} \right) \right\| \quad (34)$$

For a down-wind scheme, the term  $v_i = \frac{a}{\pi\delta^2} \mathbf{v}_i \cdot \mathbf{e}(x, \hat{x})$  is always positive. This means the real part of the complex amplification factor,  $\text{Re}(\varepsilon)$ , is always greater than 1. Therefore, the magnitude  $\|\varepsilon\|$  must be greater than 1, confirming that the down-wind scheme for the one-dimensional constant advection equation is unconditionally unstable within the PD framework.

### Appendix C. Physical Interpretation of Terms $Q_{d,ii}$ and $Q_{v,ii}$

Let's consider a simple case with only heat diffusion. For the calculation of heat flux in PD, there are two methods shown in Fig. 20 (a) and (c) of Chen et al. (2015) [45]. These two methods are mathematically equivalent.

Focusing on subfigures (b) and (d), we can see that when the temperature within the node itself is not uniform, heat transfer also occurs internally in the volume associated with the discretization node  $x_i$ , meaning the transfer between the "left" and "right" sides of the volume associated with the node. If this internal heat transfer is not considered, the calculated heat passing through the cross-section passing through  $x_i$  (which sits at the center of its nodal volume) is underestimated. Therefore, the  $Q_{d,ii}$  term is necessary. The same principle applies to  $Q_{v,ii}$ .

The volume of the node  $x_i$  is, naturally, fully covered by its horizon region. For nodes  $x_j$  in the family of neighbors of node  $x_i$ , their volume may be fully or partially covered by the horizon region of node  $x_i$ . Please see Ref. [27] for a simple algorithm that efficiently identifies the contribution of nodes partially covered by the horizon.

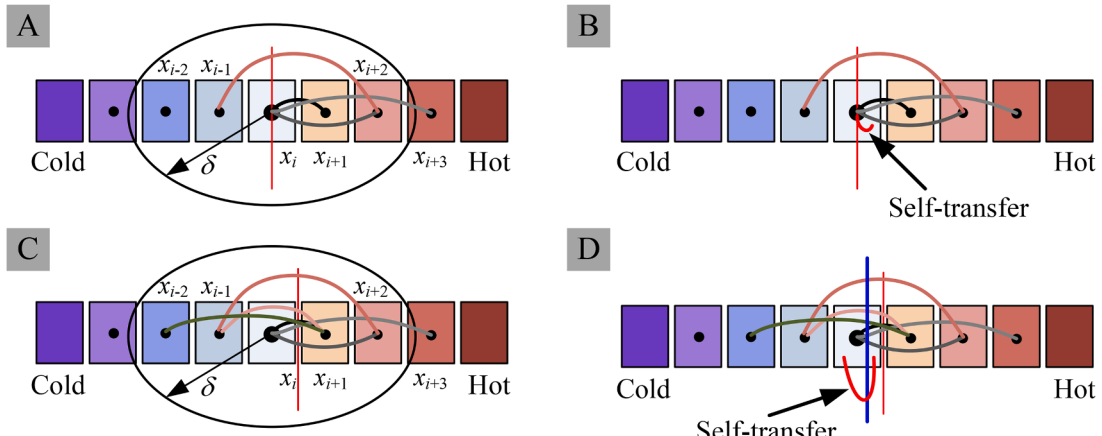


**Fig. 20.** Two different definitions of PD heat flux in (A) and (C). (A) PD heat flux is the rate at which heat is transferred through a material point across a given surface at that point, per unit area and per unit time. The thermal conductors ending at  $x_i$  from one side of the bar contribute to the heat flux at  $x_i$ , while thermal conductors like the one between the points  $x_{i+2}$  and  $x_{i-1}$ , do not. In (B), transfer (red curve) from one side of the nodal length (area in 2D, volume in 3D) to the other also contributes to the flux when the actual temperature over the nodal length is not uniform. (C) peridynamic heat flux as the rate at which heat is transferred through a given surface at a certain geometrical point. All of the bonds crossing this surface contribute to the heat flux at this point. (D) When the geometrical point (red line) moves inside a material point, the bonds cut by the surface are the same, but a "self-transfer" (red curve) inside that node has to also be included in carrying out heat through the blue line surface [45]. The horizon region is indicated in (A) and (C) by the "radius"  $\delta$ .

### Appendix D. Comparison of solid wall boundary conditions

The analysis corresponds to the example depicted in Fig. 5(b) of Section 4.1. Here, we set the  $\delta = 2$  mm and  $m = 4$ . The time step used for solving the flow velocity component is  $\Delta t_v = 0.01$  s. As illustrated in Fig. 21, the grey region represents the wall. The flow diagram reveals the presence of velocities perpendicular to the wall at the locations marked by red circles, indicating that the  $\mathbf{v} \cdot \mathbf{n} = 0$  condition is not strictly maintained in certain complex scenarios.

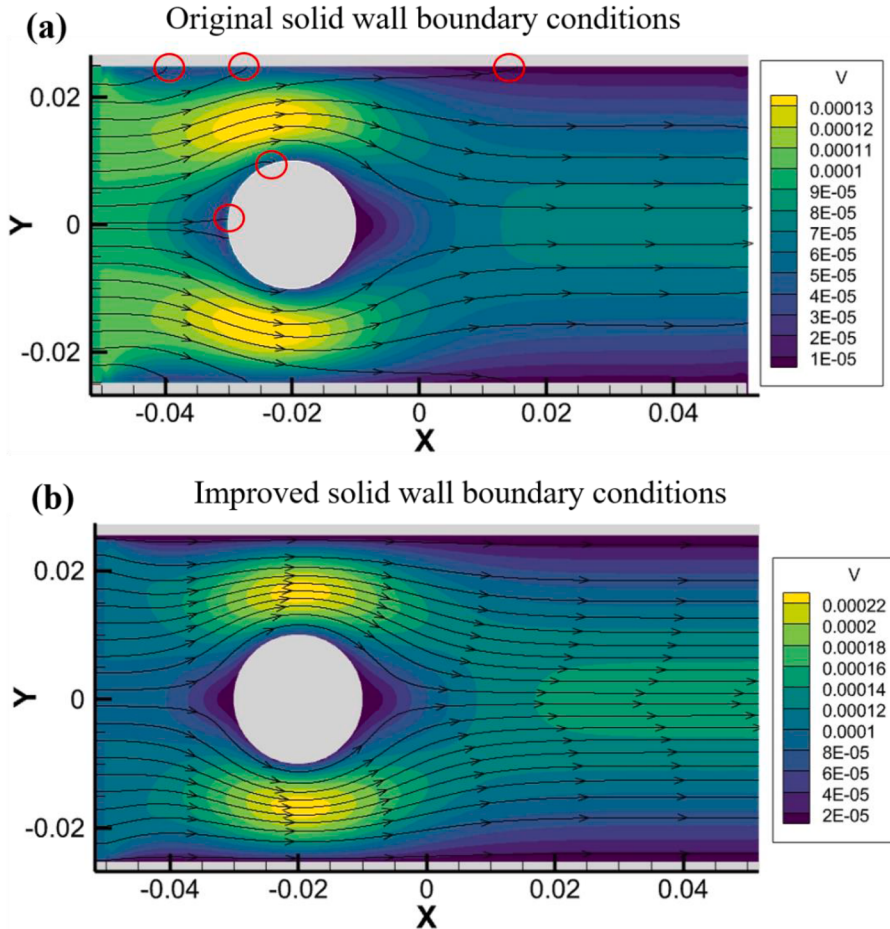


**Fig. 21.** The PD-computed velocity field for the problem of channel flow around an obstacle (see Fig. 5(b)): (a) shows the result of the no-slip solid-wall boundary condition in [51], while (b) shows the result with the improved no-slip solid-wall boundary condition in this work.

#### Appendix E. Algorithm for the Advection-Reaction-Diffusion Solver

---

```

Solver for Advection Reaction Diffusion Processes under Non uniform Flow Conditions within the PD Framework
1      (* Euler iteration loop, total_iters is the total number of iterations *)
2      Fluid = 1 (* Initialization *)
3      Δt = Δtr (* Set timestep for fluid dynamics *)
4      (* "Fluid" is a flag to determine whether to use the flow solver (1) of the
5      reaction solver (0) *)
6      For t = 1 to total_iters do
7          (* Start solving the flow field *)
8          If Fluid = 1 then
9              (* Calculate density change for each node *)
10             For i = 1 to total_nodes do
11                 Δρ = 0
12                 (* "fam" represents the number of nodes in the horizon *)
13                 For j = 1 to fam do
14                     Δρ = Δρ + fv(ρt-1) + fd(ρt-1)
15                 End for
16                 ρt = ρt-1 + ΔρΔt
17                 pt = pressure(ρt)
18                 End for
19
20             (* Calculate velocity change for each node *)
21             For i = 1 to total_nodes do
22                 Δv = 0

```

(continued on next page)

(continued)

---

```

23          (* 'node_type' represents the type of the node: 1 for liquid, 2
24          for solid *)
25          If node_type(i) = 1 then
26              For j = 1 to fam do
27                   $\Delta v = \Delta v + g(\rho^{t-1}, p^{t-1}, v^{t-1}) + b\rho^{t-1}$ 
28                  End for
29                   $v^t = v^{t-1} + \Delta v\Delta t$ 
30                  End if
31              End for
32          End if
33          (* Check for steady state based on the relative change in velocity between
34          timesteps. *)
35          If  $\epsilon(v^t, v^{t-1}) \leq 5 \times 10^{-6}$  then
36              Fluid = 0
37               $\Delta t = \Delta t_R$  (* Switch to timestep for reaction-diffusion *)
38          End if
39
40          (* Start using the Dissolution/Bimolecular Reaction solver *)
41          If Fluid = 0 then
42              For i = 1 to total_nodes do
43                  (* First, calculate the concentration change for all liquid nodes *)
44                  If node_type(i) = 1 then
45                      For m = 1 to total_liquid_species do
46                           $\Delta C_m = 0$ 
47                          For j = 1 to fam do
48                               $\Delta C_m = \Delta C_m + h_d(C_m^{t-1}) + h_v(C_m^{t-1})$ 
49                          End for
50                          (* Add the reaction term  $h_R(C_m^{t-1})$  *)
51                           $C_m^t = C_m^{t-1} + \Delta C_m \Delta t + h_R(C_m^{t-1})$ 
52                      End for
53                  End if
54
55                  (* Next, calculate the concentration change for all solid nodes *)
56                  If node_type(i) = 2 then
57                      For m = 1 to total_solid_species do
58                           $C_m^t = C_m^{t-1} + h_R(C_m^{t-1})$ 
59                      End for
60                  End if
61                  End for
62              End if
63
64              (* Check for nodes undergoing a phase change from solid to liquid *)
65              For i = 1 to total_nodes do
66                  If node_type(i) = 2 then
67                      (* If the sum of concentrations of all solid species at this node is
68                      less than or equal to zero, it indicates a phase change. *)
69                      If  $\sum C_{solid}^t \leq 0$  then
70                          node_type(i) = 1
71                           $\Delta t = \Delta t_v$ 
72                          Fluid = 1
73                      End if
74                  End if
75              End for
76          End for

```

---

## Appendix F. $\delta$ -convergence

The analysis corresponds to the example shown in Fig. 5(a) in Section 4.1. The  $\delta$ -convergence of the x-direction velocity along the line at  $x = 0$  for  $\delta = 1$  mm, 2 mm, 4 mm, 8 mm (with  $m = 4$ ) is depicted in Fig. 22, with specific convergence error detailed in Table 1. By “convergence error” here we refer to the difference between the numerical PD solution and the numerical solution (obtained with a sufficiently fine mesh in COMSOL) of the corresponding classical model. Note that the subtle discrepancy in velocity distribution near walls in Fig. 22 stems from the nonlocal model’s distinctive behavior near walls and approximation of the classical no-slip solid wall boundary condition [77–79]. This difference will gradually diminish as the horizon size approaches zero. Additionally, the  $\delta$ -convergence of the solution for the PD concentration field at 500 s is presented in Fig. 23, with specific convergence error detailed in

Table 2. The error calculation formulas in Table 1 and Table 2 are defined as  $\varepsilon_{v,r} = \sqrt{\frac{\sum_{i=1}^N (v_i^{PD} - v_i^{COMSOL})^2}{\sum_{i=1}^N (v_i^{COMSOL})^2}}$  and  $\varepsilon_{R,r} = \sqrt{\frac{\sum_{i=1}^N (C_{AB,i}^{PD} - C_{AB,i}^{COMSOL})^2}{\sum_{i=1}^N (C_{AB,i}^{COMSOL})^2}}$  respectively, where  $N$  denotes the total number of nodes used to discretize the entire domain of the problem.

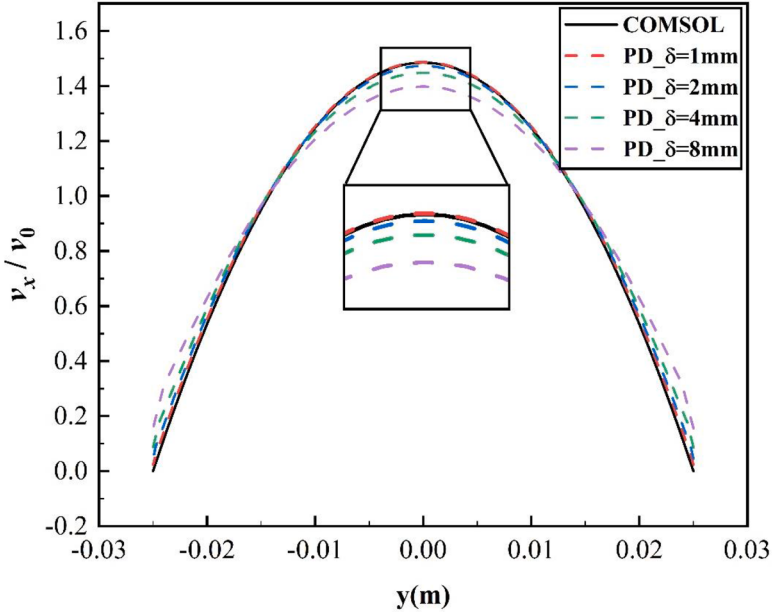


**Fig. 22.** Relative velocity at steady state in the x-direction at  $x = 0$  for the flow in a channel problem setup shown in Fig. 5(a).

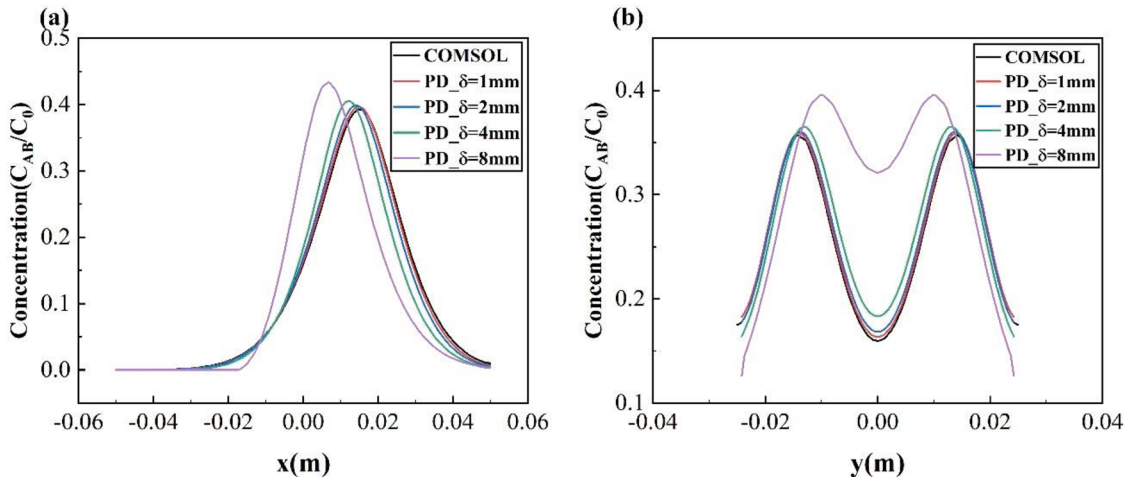


**Fig. 23.** Reactive flow in a simple channel problem (Fig. 5(a)):  $\delta$ -convergence for the concentration of product AB at  $y = 0$  and  $x = 0$  at times: (a)  $t = 500$  s, and (b)  $t = 500$  s.

**Table 1**

$\delta$ -convergence study for the PD-computed flow field for the problem in Fig. 5(a).

Error	$\delta = 8\text{ mm}$	$\delta = 4\text{ mm}$	$\delta = 2\text{ mm}$	$\delta = 1\text{ mm}$
$\varepsilon_{v,r}$	0.0802	0.0443	0.0228	0.0137

**Table 2**

$\delta$ -convergence study for the PD-computed concentration of product AB for the problem in Fig. 5(a), at different times.

$\delta$	$\varepsilon_{R,r}$ at different times							
	100 s	200 s	300 s	400 s	500 s	600 s	700 s	800 s
8 mm	0.5132	0.4150	0.3645	0.3257	0.2939	0.2677	0.2311	0.1730
4 mm	0.2318	0.1674	0.1402	0.1244	0.1137	0.1054	0.0843	0.0628
2 mm	0.1074	0.0704	0.0561	0.0496	0.0463	0.0445	0.0389	0.0397
1 mm	0.0527	0.0292	0.0219	0.0202	0.0206	0.0222	0.0238	0.0276

## Appendix G. Supplementary data

The following is the Supplementary material related to this article.

Video S1. Evolution of the dissolution of solid substance A for a Reynolds number of  $Re = 2$ . The video visualizes the corresponding evolution of the solid's geometry. This simulation corresponds to the case shown in Fig. 16(a).

Video S2. Evolution of the dissolution of solid substance A for a Reynolds number of  $Re = 10$ . The video visualizes the corresponding evolution of the solid's geometry. This simulation corresponds to the case shown in Fig. 16(b).

Video S3. Evolution of the dissolution of solid substance A for a Reynolds number of  $Re = 50$ . The video visualizes the corresponding evolution of the solid's geometry. This simulation corresponds to the case shown in Fig. 16(c).

## Data availability

Data will be made available on request.

## References

- [1] J. Naghipoor, N. Jafary, T. Rabczuk, Mathematical and computational modeling of drug release from an ocular iontophoretic drug delivery device, *Int J Heat Mass Transf* 123 (2018) 1035–1049.
- [2] S.J. Chapman, R.J. Shipley, R. Jawad, Multiscale Modeling of Fluid Transport in Tumors, *Bull. Math. Biol.* 70 (2008) 2334–2357.
- [3] V. Guvanasen, R.E. Volker, Numerical solutions for solute transport in unconfined aquifers, *Int J Numer Methods Fluids* 3 (2010) 103–123.
- [4] D. Brockmann, D. Helbing, The Hidden Geometry of Complex, Network-Driven Contagion Phenomena, *Science* 342 (2013) 1337–1342.
- [5] C.L.N. Cunha, J.A.M. Carrer, M.F. Oliveira, V.L. Costa, A study concerning the solution of advection–diffusion problems by the Boundary Element Method, *Eng Anal Bound Elem* 65 (2016) 79–94.
- [6] F. Guillén-González, J.V. Gutiérrez-Santacreu, Error estimates of a linear decoupled Euler–FEM scheme for a mass diffusion model, *Numer. Math.* 117 (2011) 333–371.
- [7] M. Dehghan, Weighted finite difference techniques for the one-dimensional advection–diffusion equation, *Appl. Math. Comput.* 147 (2004) 307–319.
- [8] A.D. Rubio, A. Zalts, C.D. El Hasi, Numerical solution of the advection–reaction–diffusion equation at different scales, *Environ. Model. Softw.* 23 (2008) 90–95.
- [9] C.M. Gralming, C.F. Harvey, L.C. Meigs, Reactive Transport in Porous Media: a Comparison of Model Prediction with Laboratory Visualization, *Env. Sci. Technol.* 36 (2002) 2508–2514.
- [10] D.S. Raje, V. Kapoor, Experimental study of bimolecular reaction kinetics in porous media, *Env. Sci. Technol.* 34 (2000) 1234–1239.
- [11] A. Walicka, B. Iwanowska-Chomiak, Drug diffusion transport through human skin, *Int. J. Appl. Mech. Eng.* 23 (2018) 977–988.
- [12] S. Karra, D. O’Malley, J. Hyman, H.S. Viswanathan, G. Srinivasan, Modeling flow and transport in fracture networks using graphs, *Phys. Rev. E* 97 (2018) 033304.
- [13] K.G. Manjari, G.S. Babu, Reliability and sensitivity analyses of discrete fracture network based contaminant transport model in fractured rocks, *Comput. Geotech.* 145 (2022) 104674.
- [14] Z. Chen, F. Bobaru, Peridynamic modeling of pitting corrosion damage, *J Mech Phys Solids* 78 (2015) 352–381.
- [15] C. Tian, J. Du, S. Fan, Z. Chen, A general electrochemical peridynamic model for corrosion and electrodeposition, *J. Electroanal. Chem.* 968 (2024) 118512.
- [16] X.-P. Xu, A. Needleman, Numerical simulations of fast crack growth in brittle solids, *J Mech Phys Solids* 42 (1994) 1397–1434.
- [17] X. Wang, B. Wang, M. Meyerson, C.B. Mullins, Y. Fu, L. Zhu, L. Chen, A phase-field model integrating reaction-diffusion kinetics and elasto-plastic deformation with application to lithiated selenium-doped germanium electrodes, *Int. J. Mech. Sci.* 144 (2018) 158–171.
- [18] T. Belytschko, R. Gracie, G. Ventura, A review of extended/generalized finite element methods for material modeling, *Model. Simul. Mater. Sci. Eng.* 17 (2009) 043001.
- [19] H. Sun, Y. Wang, L. Yu, X. Yu, A discussion on nonlocality: from fractional derivative model to peridynamic model, *Commun. Nonlinear Sci. Numer. Simul.* 114 (2022) 106604.
- [20] X.-R. Yang, Y. Wang, Ubiquity of anomalous transport in porous media: numerical evidence, continuous time random walk modelling, and hydrodynamic interpretation, *Sci Rep* 9 (2019) 4601.
- [21] R. Metzler, J. Klafter, The random walk’s guide to anomalous diffusion: a fractional dynamics approach, *Phys Rep* 339 (2000) 1–77.
- [22] K.J. Painter, T. Hillen, J.R. Potts, Biological modeling with nonlocal advection–diffusion equations, *Math. Models Methods Appl. Sci.* 34 (2024) 57–107.
- [23] L. Mei, X. Zhang, Existence and nonexistence of positive steady states in multi-species phytoplankton dynamics, *J Differ Equ* 253 (2012) 2025–2063.
- [24] M. Yamaguchi, E. Yoshimoto, S. Kondo, Pattern regulation in the stripe of zebrafish suggests an underlying dynamic and autonomous mechanism, *Proc. Natl. Acad. Sci.* 104 (2007) 4790–4793.
- [25] S.A. Silling, Reformulation of elasticity theory for discontinuities and long-range forces, *J Mech Phys Solids* 48 (2000) 175–209.
- [26] S.A. Silling, R.B. Lehoucq, Peridynamic theory of solid mechanics, *Adv. Appl. Mech.* 44 (2010) 73–168.
- [27] F. Bobaru, G. Zhang, Why do cracks branch? A peridynamic investigation of dynamic brittle fracture, *Int. J. Fract.* 196 (2015) 59–98.
- [28] F. Bobaru, J.T. Foster, P.H. Geubelle, S.A. Silling, *Handbook of peridynamic modeling*, CRC Press, 2016.
- [29] Z. Chen, S. Niazi, F. Bobaru, A peridynamic model for brittle damage and fracture in porous materials, *Int. J. Rock Mech. Min. Sci.* 122 (2019) 104059.
- [30] Y.D. Ha, F. Bobaru, Characteristics of dynamic brittle fracture captured with peridynamics, *Eng Fract Mech* 78 (2011) 1156–1168.
- [31] D. Huang, G. Lu, P. Qiao, An improved peridynamic approach for quasi-static elastic deformation and brittle fracture analysis, *Int. J. Mech. Sci.* 94 (2015) 111–122.
- [32] J. Mehrmashhad, M. Bahadori, F. Bobaru, On validating peridynamic models and a phase-field model for dynamic brittle fracture in glass, *Eng Fract Mech* 240 (2020) 107355.
- [33] H. Ouchi, A. Katiyar, J. York, J.T. Foster, M.M. Sharma, A fully coupled porous flow and geomechanics model for fluid driven cracks: a peridynamics approach, *Comput Mech* 55 (2015) 561–576.
- [34] P. Nikolaev, A.P. Jivkov, M. Fifre, M. Sedighi, Peridynamic analysis of thermal behaviour of PCM composites for heat storage, *Comput Methods Appl Mech Eng* 424 (2024) 116905.
- [35] S.A. Silling, A. Askari, *Peridynamic Model For Fatigue Cracking*, Sandia National Lab.(SNL-NM), Albuquerque, NM (United States), 2014.
- [36] G. Zhang, Q. Le, A. Loghin, A. Subramanyan, F. Bobaru, Validation of a peridynamic model for fatigue cracking, *Eng Fract Mech* 162 (2016) 76–94.
- [37] E. Madenci, S. Oterkus, Ordinary state-based peridynamics for plastic deformation according to von Mises yield criteria with isotropic hardening, *J Mech Phys Solids* 86 (2016) 192–219.
- [38] J.T. Foster, S.A. Silling, W.W. Chen, Viscoplasticity using peridynamics, *Int J Numer Methods Eng* 81 (2010) 1242–1258.
- [39] W. Dong, H. Liu, J. Du, X. Zhang, M. Huang, Z. Li, Z. Chen, F. Bobaru, A peridynamic approach to solving general discrete dislocation dynamics problems in plasticity and fracture: part II. Applications, *Int. J. Plast.* 159 (2022) 103462.

- [40] F. Mousavi, S. Jafarzadeh, F. Bobaru, A fast convolution-based method for peridynamic models in plasticity and ductile fracture, *Int. J. Fract.* 249 (2025) 1–31.
- [41] S. Jafarzadeh, Z. Chen, J. Zhao, F. Bobaru, Pitting, lacy covers, and pit merger in stainless steel: 3D peridynamic models, *Corros Sci* 150 (2019) 17–31.
- [42] J. Zhao, Z. Chen, J. Mehrmashhadi, F. Bobaru, A stochastic multiscale peridynamic model for corrosion-induced fracture in reinforced concrete, *Eng Fract Mech* 229 (2020) 106969.
- [43] P. Wu, J. Zhao, Z. Chen, F. Bobaru, Validation of a stochastically homogenized peridynamic model for quasi-static fracture in concrete, *Eng Fract Mech* 237 (2020) 107293.
- [44] J. Mehrmashhadi, Z. Chen, J. Zhao, F. Bobaru, A stochastically homogenized peridynamic model for intraply fracture in fiber-reinforced composites, *Compos Sci Technol* 182 (2019) 107770.
- [45] Z. Chen, F. Bobaru, Selecting the kernel in a peridynamic formulation: a study for transient heat diffusion, *Comput Phys Commun* 197 (2015) 51–60.
- [46] J. Zhao, Z. Chen, J. Mehrmashhadi, F. Bobaru, Construction of a peridynamic model for transient advection-diffusion problems, *Int J Heat Mass Transf* 126 (2018) 1253–1266.
- [47] C. Tian, S. Fan, J. Du, Z. Zhou, Z. Chen, F. Bobaru, A peridynamic model for advection–reaction–diffusion problems, *Comput Methods Appl Mech Eng* 415 (2023) 116206.
- [48] E. Madenci, A. Barut, M. Futch, Peridynamic differential operator and its applications, *Comput Methods Appl Mech Eng* 304 (2016) 408–451.
- [49] Y. Gao, S. Oterkus, Nonlocal numerical simulation of low Reynolds number laminar fluid motion by using peridynamic differential operator, *Ocean Eng.* 179 (2019) 135–158.
- [50] H. Chang, A. Chen, A. Kareem, L. Hu, R. Ma, Peridynamic differential operator-based Eulerian particle method for 2D internal flows, *Comput Methods Appl Mech Eng* 392 (2022) 114568.
- [51] J. Zhao, A. Larios, F. Bobaru, Construction of a peridynamic model for viscous flow, *J Comput Phys* 468 (2022) 111509.
- [52] S. Patankar, *Numerical Heat Transfer and Fluid Flow*, CRC Press, 1980, Chapter 5.
- [53] M. Antuono, A. Colagrossi, S. Marrone, D. Molteni, Free-surface flows solved by means of SPH schemes with numerical diffusive terms, *Comput Phys Commun* 181 (2010) 532–549.
- [54] D.H. Zhang, Y.X. Shi, C. Huang, Y.L. Si, B. Huang, W. Li, SPH method with applications of oscillating wave surge converter, *Ocean Eng.* 152 (2018) 273–285.
- [55] F. Bobaru, M. Duangpanya, A peridynamic formulation for transient heat conduction in bodies with evolving discontinuities, *J Comput Phys* 231 (2012) 2764–2785.
- [56] J.J. Monaghan, Simulating Free Surface Flows with SPH, *J Comput Phys* 110 (1994) 399–406.
- [57] S.A. Silling, E. Askari, A meshfree method based on the peridynamic model of solid mechanics, *Comput Struct* 83 (2005) 1526–1535.
- [58] X. Gu, Q. Zhang, X. Xia, Voronoi-based peridynamics and cracking analysis with adaptive refinement, *Int J Numer Methods Eng* 112 (2017) 2087–2109.
- [59] S.F. Henke, S. Shanbhag, Mesh sensitivity in peridynamic simulations, *Comput Phys Commun* 185 (2014) 181–193.
- [60] F. Bobaru, Y.D. Ha, Adaptive refinement and multiscale modeling in 2D peridynamics, *Int. J. Multiscale Comput. Eng.* 9 (2011) 635–660.
- [61] S. Li, Z. Chen, L. Tan, F. Bobaru, Corrosion-induced embrittlement in ZK60A Mg alloy, *Mater. Sci. Eng.: A* 713 (2018) 7–17.
- [62] S. Jafarzadeh, F. Mousavi, A. Larios, F. Bobaru, A general and fast convolution-based method for peridynamics: applications to elasticity and brittle fracture, *Comput Methods Appl Mech Eng* 392 (2022).
- [63] S. Jafarzadeh, L. Wang, A. Larios, F. Bobaru, A fast convolution-based method for peridynamic transient diffusion in arbitrary domains, *Comput Methods Appl Mech Eng* 375 (2021).
- [64] S. Jafarzadeh, A. Larios, F. Bobaru, Efficient Solutions for Nonlocal Diffusion Problems Via Boundary-Adapted Spectral Methods, *J. Peridynamics Nonlocal Model.* 2 (2020) 85–110.
- [65] W. Hu, Y.D. Ha, F. Bobaru, Peridynamic model for dynamic fracture in unidirectional fiber-reinforced composites, *Comput Methods Appl Mech Eng* 217–220 (2012) 247–261.
- [66] H. Liu, Z. Chen, On the one-point quadrature discretization in peridynamics: a novel perspective from Monte Carlo integration, *Comput Phys Commun* 298 (2024) 109115.
- [67] F. Bobaru, M. Duangpanya, The peridynamic formulation for transient heat conduction, *Int. J. Heat Mass Transf.* 53 (2010) 4047–4059.
- [68] P. Seleson, Improved one-point quadrature algorithms for two-dimensional peridynamic models based on analytical calculations, *Comput Methods Appl Mech Eng* 282 (2014) 184–217.
- [69] Y. Tao, X. Tian, Q. Du, Nonlocal diffusion and peridynamic models with Neumann type constraints and their numerical approximations, *Appl Math Comput* 305 (2017) 282–298.
- [70] S. Oterkus, E. Madenci, A. Agwai, Peridynamic thermal diffusion, *J Comput Phys* 265 (2014) 71–96.
- [71] Q. Du, M. Gunzburger, R.B. Lehoucq, K. Zhou, A nonlocal vector calculus, nonlocal volume-constrained problems, and nonlocal balance laws, *Math. Models Methods Appl. Sci.* 23 (2013) 493–540.
- [72] Q.V. Le, F. Bobaru, Surface corrections for peridynamic models in elasticity and fracture, *Comput Mech* 61 (2017) 499–518.
- [73] J. Zhao, S. Jafarzadeh, Z. Chen, F. Bobaru, Enforcing local boundary conditions in peridynamic models of diffusion with singularities and on arbitrary domains, *Eng Comput* 41 (2025) 247–266.
- [74] C.T. Nguyen, S. Oterkus, E. Oterkus, I. Amin, M. Ozdemir, A.-H. El-Aassar, H. Shawky, Modelling of Eulerian incompressible fluid flows by using peridynamic differential operator, *Ocean Eng.* 239 (2021) 109815.
- [75] F. Bobaru, M. Yang, L.F. Alves, S.A. Silling, E. Askari, J. Xu, Convergence, adaptive refinement, and scaling in 1D peridynamics, *Int J Numer Methods Eng* 77 (2008) 852–877.
- [76] A. Rahmat, M. Barigou, A. Alexiadis, Numerical simulation of dissolution of solid particles in fluid flow using the SPH method, *Int. J. Numer. Methods Heat Fluid Flow* 30 (2020) 290–307.
- [77] A.C. Eringen, Micromorphic theory of turbulence, *Z. angew. Math. Phys.* 61 (2009) 119–132.
- [78] A.C. Eringen, Incompressible micromorphic fluid model for turbulence, *Int J Eng Sci* 41 (2003) 1041–1057.
- [79] A.C. Eringen, Memory-dependent orientable nonlocal micropolar fluids, *Int J Eng Sci* 29 (1991) 1515–1529.